

Climate change impacts on tropical cyclones of the Arabian Sea: Projections and uncertainty investigations

Zahra Ranji¹  | Amin Reza Zarifsanayei^{2,3} | Nick Cartwright^{2,3} | Mohsen Soltanpour¹

¹Department of Civil Engineering, KN Toosi University of Technology, Tehran, Iran

²School of Engineering and Built Environment, Griffith University, Gold Coast, Queensland, Australia

³Coastal and Marine Research Centre (CMRC), Griffith University, Gold Coast, Queensland, Australia

Correspondence

Zahra Ranji, Department of Civil Engineering, KN Toosi University of Technology, Tehran, Iran.
Email: zranji@mail.kntu.ac.ir

Abstract

This study investigates some of the uncertainties sources associated with the pseudo global warming (PGW) approach which was employed to project future patterns of tropical cyclones (TCs) over the Arabian Sea (AS). First, the climate variables controlling the patterns of tropical cyclones were extracted from reanalysis datasets of ERA5, ERAI, CFSR, and NCEP/NCAR. Then, each dataset was evaluated against long-term measurements to identify the best-performing reanalysis dataset. ERA5 showed the best performance for most of the variables. Outputs of 20 CMIP5 global climate models (GCMs) were then evaluated against the ERA5 data resulting in an ensemble of the best performing GCMs. A PGW framework was then used to project the changes in patterns of three significant historical cyclones: Gonu, Phet, and Ashobaa. In doing so, the signals of future climate variables were extracted from the GCMs ensemble to modify the initial and boundary conditions of the WRF model which was previously tuned for reproducing the historical TCs. Different tests were conducted to address the sources of uncertainty in the PGW approach, including the selection of the climate variables contributing to the computation of the signals, the selection of GCMs, and the spatial variation of signals. A considerable sensitivity of the projected track and intensity of TCs to the choice of GCMs was observed, acknowledging the importance of GCMs evaluation before calculating the signals. Moreover, it was found that among all variables, signals of sea surface temperature and air temperature have major effects on the cyclone's track and intensity. Apart from that, when the signals were applied to the domain of the WRF model uniformly, compared to applying spatially varying signals, different tracks and intensities for future TCs were also observed. Overall, the findings of this paper challenge the reliability of the projected changes in TCs patterns obtained from PGW.

KEY WORDS

climate models, pseudo global warming, tropical cyclones, WRF

1 | INTRODUCTION

The northern Indian Ocean includes two major basins, the Bay of Bengal and the Arabian Sea (AS). Cycles of reversal of monsoon winds blow from northeast (NE) and southwest (SW) in different seasons over the AS. NE (winter) monsoon exists throughout November to February that is followed by a transient season. SW (summer) monsoon onsets during June and lasts till the end of September. Monsoon winds can change in response to climate change (hereafter CC) impacts (Parvathi *et al.*, 2017). Tropical cyclones (TCs) and TC-driven waves and surges in the AS have also shown some changes under the effects of CC, resulting in TC intensification over recent decades. More recently, Deshpande *et al.* (2021) reported a remarkable increase in the frequency, intensity, and duration of TCs in the AS compared to the Bay of Bengal. These increases are much greater for more intense TCs, which are associated with the increase in mid-level relative humidity and column averaged moist static energy, the factors that are correlated with the increase of sea surface temperature (SST) in the basin. To a certain extent, these intensifications are related to an upward trend in anthropogenic black carbon and sulphate emissions (Evan and Camargo, 2011), which are likely to increase by 2100 (Knutson *et al.*, 2010). Evan and Camargo (2011) stated that increasing anthropogenic emissions of aerosols leads to weakening of vertical wind shear that causes TC intensification in premonsoon and postmonsoon seasons in the AS. Murakami *et al.* (2013) indicated that projected TC frequency increases in the northern AS by about 46%, with a robust increase over land areas, showing the greater potential damage in these regions. Knutson *et al.* (2015) projected a 200% increase in the occurrence of category 4–5 TCs over the north Indian Ocean, under RCP4.5 in the late 21st century. Bell *et al.* (2020) pointed out that TC genesis frequency in the northern AS is likely to increase in the premonsoon season, consistent with changes in relative humidity and vertical wind shear.

In general, recent studies revealed that due to CC impacts, there is a significant increase in the risks of TCs (e.g., Walsh *et al.*, 2018) and the respective subsequences, for example, inundations (Sajjad *et al.*, 2020) and flash floods (Zhang *et al.*, 2019). However, Global Climate Models (GCMs) cannot adequately capture TCs because of their coarse spatial resolutions compared to the size of a TC core. Different approaches have been developed so far to analyse the response of TCs to CC:

- Downscaling global climate models to regional climate models, using statistical methods (e.g., Jones *et al.*, 2016).
- GCM-driven statistical/deterministic hurricane models (e.g., Lin *et al.*, 2012).

- Pseudo global warming (PGW) approach (e.g., Mäll *et al.*, 2020).

In the third approach, absolute differences between the future and baseline of the climate variables, hereafter termed signals, are extracted from GCM projections. Then, the signals are used to change the input (i.e., initial and boundary conditions) of a numerical model (i.e., the Weather Research and Forecasting model, WRF) utilized for hindcasting TCs. The results of the model are then presented as the future projection of the TC.

Addressing uncertainty is a prerequisite for conducting reliable CC studies and developing future coastal hazard mitigation plans (e.g., Zarifsanayei *et al.*, 2022). Generally, the TC projections obtained from the PGW approach are first influenced by the signals used for the initial and boundary conditions of the WRF model. The computation of signals is uncertain due to the selection of RCPs, GCMs, climate variables, and spatiotemporal resolutions used for introducing the signals to the WRF model. The simulated TC patterns are also impacted by the settings of the WRF model (e.g., the physic schemes, type of nesting).

There are a few studies in the literature that tried to partially address the uncertainty of PGW simulations. In the most straightforward PGW approach, Mori and Takemi (2016) and Strachan *et al.* (2013) only considered sea surface temperature perturbation under the worst emission scenario. Adding atmospheric temperature and relative humidity, Nakamura *et al.* (2016) investigated CC impacts on typhoon Haiyan. Chen *et al.* (2020) and Ninomiya *et al.* (2017) excluded wind speeds from the input signals, as they lead to a significant shift of TC tracks. In some PGW studies, the input signals were averaged over the domain before being added to the initial and boundary conditions of the atmosphere model (e.g., Jisan *et al.*, 2018; Thompson *et al.*, 2021). On the other hand, some studies accounted for the spatial and temporal variability of the input signals (e.g., Mittal *et al.*, 2019; Nayak and Takemi, 2019). More recently, for better projection of future TCs and the resulting waves, surges, and inundation, an ensemble of CMIP5 models, rather than an individual GCM, was preferably used (e.g., Michaelis *et al.*, 2017; Mäll *et al.*, 2020). In a very comprehensive approach, Gutmann *et al.* (2018) utilized input signals of several variables, including zonal and meridional wind speed, sea level pressure, geopotential height, air temperature, relative humidity, and sea surface temperature, as well as initial soil temperatures and the bottom boundary condition in the soil. The mean ensemble of CMIP5 models was used to compute the signals, which were subsequently added to the boundary

condition of the WRF model, spatially and temporally. However, quantifying the uncertainty of PGW simulations still requires more effort.

In this paper, as the first step toward the projection of TCs in the AS, 20 GCMs of CMIP5 were evaluated in the AS, through extensive observational and reanalysis datasets. The best-performing GCMs were then utilized to extract the signals of the selected climate variables. The climate variables were chosen given the limitation of the input variables for the WRF model, including air temperature, relative humidity, wind speeds, and geopotential height. Other variables affecting the TCs, such as vertical wind shear, atmospheric instability, relative vorticity, and current precipitation, could not be considered here. Using the PGW approach, future projection of TCs, in two time slices of near future, that is, 2025–2045, and the far future, that is, 2080–2100 was then investigated. To this end, the three TCs of Gonu, Phet, and Ashobaa, which were previously reproduced in the baseline period (Soltanpour *et al.*, 2021) were discussed. We also provide an uncertainty analysis, to address and quantify the sources that change PGW projection significantly.

The remainder of this paper is broken down as follows. First, the research framework is presented. Then, the patterns of TCs, as well as climate variables, are discussed using field measurements. Then, available reanalysis datasets are evaluated to determine the best-fitted data. Afterwards, CMIP5 GCMs are validated by the best-performing reanalysis dataset in the baseline period to create an ensemble of the best GCMs for the projection of future climate variables. Finally, the projected changes in the patterns of TCs under different emission scenarios of CMIP5 are discussed. Sixteen different simulations with different input signals are also presented to address some uncertainties that influence the PGW outputs.

2 | DATA AND METHODS

2.1 | Field measurements

Several data sources, including the Iran Meteorological Organization (IMO, 2020), IOWA State University (IOWA State University, 2020), and NCEI of NOAA (NCEI GIS Agile Team, 2020), present measured atmospheric data for stations around the AS. Figure 1 depicts the location of deployed stations with a 3-hourly temporal resolution. According to Table 1, the stations covering the time slice of 1985–2005 included in this study are either located on land (with a maximum distance of 5 km from the coastline) or in the ocean. This set of long-term measurements was utilized to better understand the present climate and evaluate the available reanalysis datasets. Since altimeter data were formerly included in reanalysis datasets, they were not considered in the current sets of measurements. Furthermore, to check the quality of data in terms of data completeness, the method of Cordero *et al.* (2011) was utilized, in which the months with more than 6 days missing data were omitted.

The annual average temperature of all stations shows an increase of 0.9°C in the mean surface temperature within the timescale of 40 years (Figures S1–S3, Supporting Information). Figure 2 depicts the seasonal average of measured variables. In spring and summer, low pressure and high surface temperature dominate the basin. Indian stations show smooth variability of surface temperature (26–27°C) in different seasons, while the northern and western stations present significant changes from summer (30°C) to winter (22°C). During autumn and winter, a slight variability was also found for sea level pressure at northern, western, and eastern stations. Maximum relative humidity occurs in summer when the

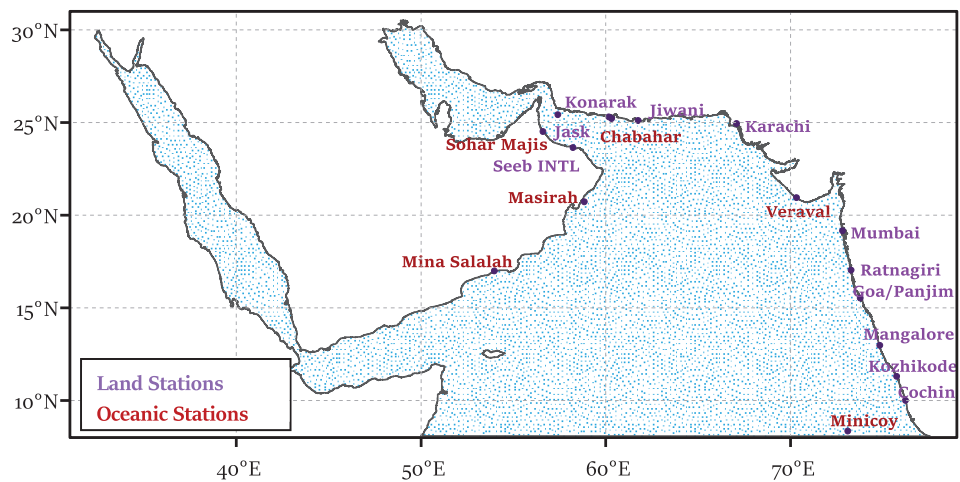


FIGURE 1 Synoptic stations along the AS coastline (Iran, Pakistan, India, and Oman) [Colour figure can be viewed at wileyonlinelibrary.com]

Station	Longitude	Latitude	Measurement period	Source
Chabahar	60.37	25.17	1987–2008	IMO
Jask	57.46	25.38	1985–2010	IMO
Konarak	60.22	25.26	1984–2005	IMO
Cochin	76.27	9.95	1944–2020	NCEI-NOAA
Goa_Panjim	73.82	15.48	1973–2020	NCEI-NOAA
Jiwani	61.81	25.07	1944–2020	NCEI-NOAA
Kozhikode	75.78	11.25	1944–2020	NCEI-NOAA
Masirah	58.89	20.68	1943–2020	NCEI-NOAA
Mina Salalah	54.02	16.93	1983–2020	NCEI-NOAA
Minicoy	73.15	8.30	1944–2020	NCEI-NOAA
Ratnagiri	73.33	16.98	1944–2020	NCEI-NOAA
Seeb INTL	58.28	23.59	1944–2020	NCEI-NOAA
Sohar Majis	56.65	24.47	1983–2020	NCEI-NOAA
Veraval	70.37	20.90	1944–2020	NCEI-NOAA
Mumbai	72.86	19.10	1945–2020	IOWA
Karachi	67.13	24.90	1942–2020	IOWA
Mangalore	74.88	12.92	1973–2020	IOWA

TABLE 1 Field measurement details of surface variables

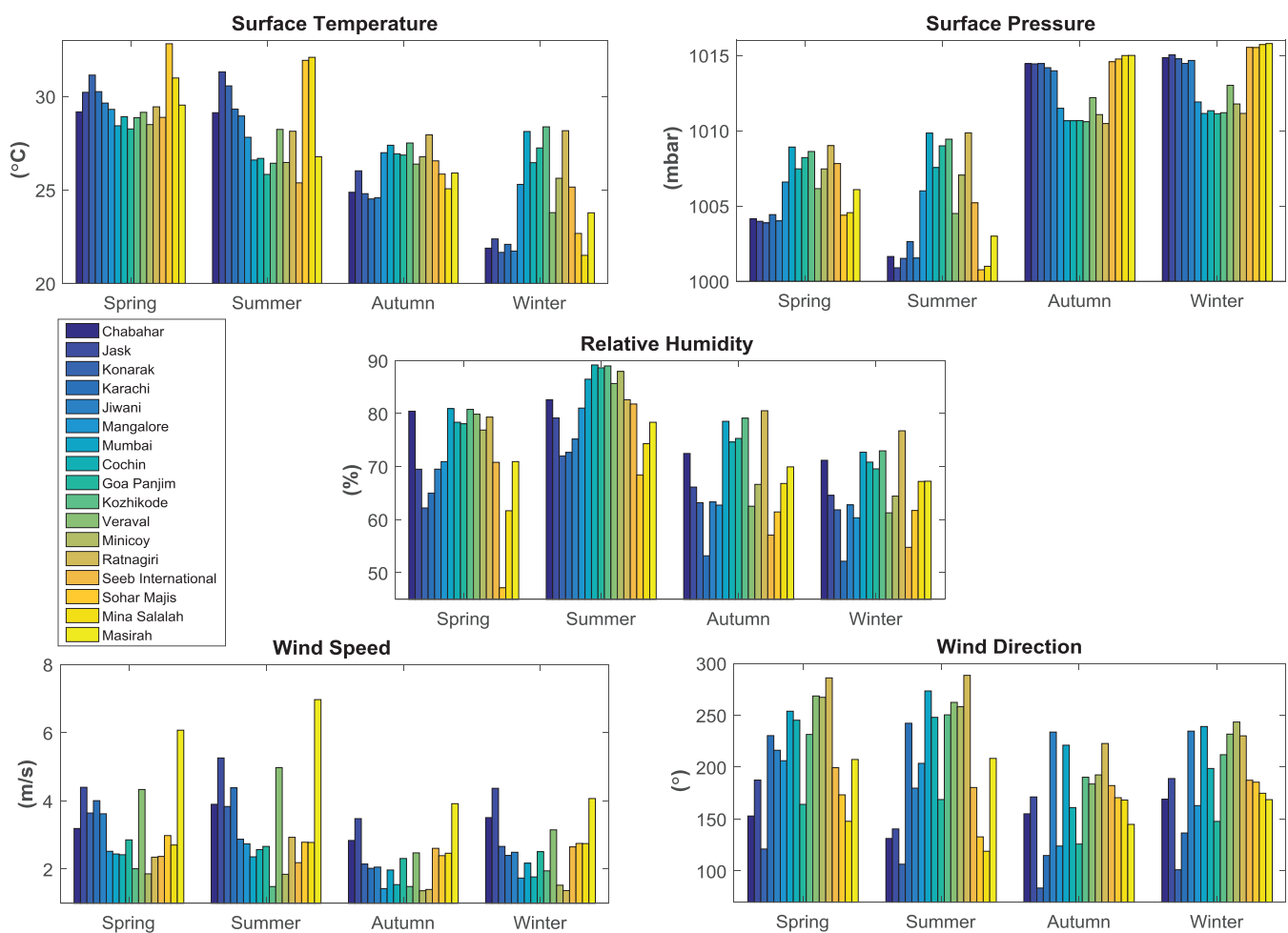


FIGURE 2 Seasonal average of measured surface temperature (top left), surface pressure (top right), relative humidity (centre), wind speed (bottom left), and wind direction (bottom right) [Colour figure can be viewed at wileyonlinelibrary.com]

eastern stations usually have larger average humidity than the northern and western stations. Typically, during monsoon seasons, the SW winds are more intense than NE winds. It was also observed that wind speeds increase in the latitudes higher than 24.5°.

Analysing wind roses of all stations around the AS reveals that west and northwest winds are dominant along the eastern coastlines. SW winds, on the other hand, dominate in the western and northern coastlines. Resultant winds in the stations close to the Strait of Hormuz (e.g., Jask) mostly come from east–west (Figures S1–S3).

Seasonal wind roses show that west winds dominate in the eastern coastlines for all seasons. Observed wind roses in spring and summer, and in autumn and winter, are similar. NE winds in the western coastlines and east winds in the eastern coastlines are dominant in autumn and winter. In the summer monsoon, wind direction changes along the northwestern and eastern coasts of the AS. Regardless, the SW direction is observed in other stations. Comparing yearly and summer wind roses, it was found out that SW winds considerably influence the wind climate over the AS (Figures S1–S3).

Favourable conditions for the generation of TCs (i.e., higher temperature, relative humidity, wind speeds, and lower pressure) during summer, within the study area, do not necessarily yield a higher frequency of occurrence for TC because TCs activity depends on different climate variabilities such as the El Niño–Southern Oscillation and Indian Ocean Dipole (Sattar and Cheung, 2019).

Bimodal TC activity in the north Indian Ocean includes the premonsoon (May–June: spring) and postmonsoon (October–November: autumn) seasons. It is also asymmetric between the AS and Bay of Bengal basins, mainly caused by the variability of the NE monsoon (Sattar and Cheung, 2019). Balaji *et al.* (2018) reported a remarkable increase in the frequency and duration of intense cyclones together with a decreasing trend in total frequency. A general decrease in the

decadal frequency trend is also reported for cyclonic disturbances in monsoon, premonsoon, and postmonsoon seasons from the 1970s in the AS and Bay of Bengal (Gupta *et al.*, 2019). Premonsoon TCs are also intensified over the AS, according to the epochal variability in the storm ambient vertical wind shear and tropical cyclone heat potential (Rajeevan *et al.*, 2013). The probability of postmonsoon intense TCs is also increased by the effect of anthropogenic global warming over the AS (Murakami *et al.*, 2017). TCs are less active during the summer monsoon due to the suppression of TC cyclogenesis by strong wind shear. The monthly frequency of TC occurrence over the AS is shown in Figure 3 and confirms that the probability of TC occurrence increases in premonsoon and postmonsoon seasons. The highest frequency of severe cyclonic storms is identified in June. TC intensity evolves because of many factors, such as initial intensity, the thermodynamic state of the atmosphere through the track, vertical wind shear, and the heat exchange between the atmosphere and the upper layer of the ocean. June TCs are coincident with the onset of the SW monsoon, and Evan and Camargo (2011) stated that premonsoon TCs are intensified regarding a significant reduction in storm-ambient vertical wind shear as a result of increased anthropogenic black carbon and sulphate emissions. However, Wang *et al.* (2012) argued that the earlier occurrences of TCs in the recent epoch, which can be attributed to the increased low-level cyclonic shear vorticity, is the main reason for this intensification.

2.2 | Reanalysis datasets

Previous studies have evaluated GCMs performance by various approaches, such as employing a grid of measured data (e.g., Zha *et al.*, 2020) or reanalysis datasets (e.g., Morim *et al.*, 2020). In the latter approach, the performance of the reanalysis datasets should be first assessed

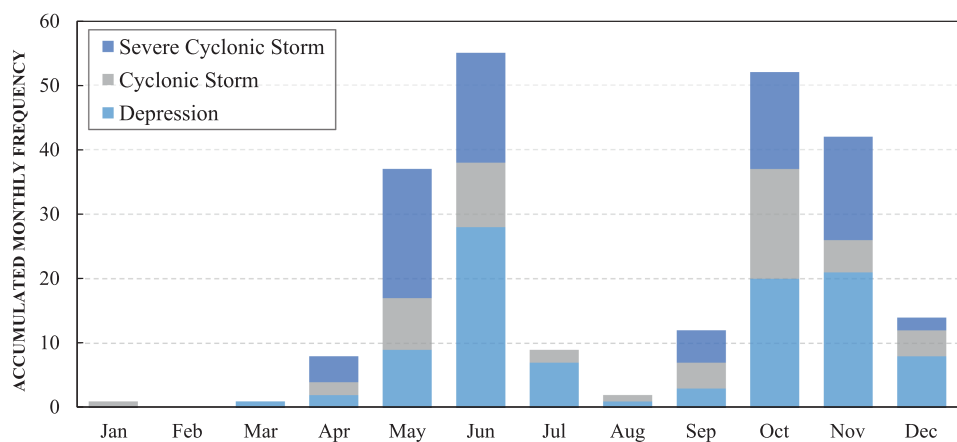


FIGURE 3 Accumulated monthly frequency of TCs over the AS within 1891–2020 (adopted from IMD, 2019) [Colour figure can be viewed at wileyonlinelibrary.com]

(Morim *et al.*, 2018). Here, four climate reanalysis datasets, ERA Interim (ERA1), ERA5, NCEP/NCAR, and CFSR (Table 2), were compared with long-term measurements of surface variables to determine the best performing dataset for the study area. The evaluation period covered the time slice of 1985–2005, when data from both reanalysis datasets and observations were available. The most accurate dataset was used later as the reference data to assess GCMs' performance and select the best-performing GCMs.

Monthly reanalysis data at the location of synoptic stations were obtained by applying bilinear interpolations. They were then compared to the measurements using different statistical indices, that is, correlation coefficient (CCF), centred root-mean-square difference (RMSD-unbiased RMSE), and standard deviation (*SD*), as defined in Equations (1)–(5),

$$SD = \sqrt{\frac{\sum_{t=1}^N (\text{ref}_t - \bar{\text{ref}})^2}{N}} \text{ or } \sqrt{\frac{\sum_{t=1}^N (\text{sim}_t - \bar{\text{sim}})^2}{N}}, \quad (1)$$

$$RMSE = \sqrt{\frac{\sum_{t=1}^N (\text{ref}_t - \text{sim}_t)^2}{N}}, \quad (2)$$

$$\text{bias} = \bar{\text{ref}} - \bar{\text{sim}}, \quad (3)$$

$$RMSD = \sqrt{\frac{\sum_{t=1}^N [(\text{ref}_t - \bar{\text{ref}}) - (\text{sim}_t - \bar{\text{sim}})]^2}{N}} = RMSE - bias, \quad (4)$$

$$CCF = \frac{\sum_{t=1}^N (\text{ref}_t - \bar{\text{ref}})(\text{sim}_t - \bar{\text{sim}})}{\sqrt{N \sum_{t=1}^N (\text{ref}_t - \bar{\text{ref}})^2 \sum_{t=1}^N (\text{sim}_t - \bar{\text{sim}})^2}}. \quad (5)$$

N represents the number of data, *ref* is the measured data, and *sim* is the reanalysis data. The least differences between *ref* and *sim* were considered for computing these indices for wind direction. For some stations, ERAI, and

ERA5 datasets, which did not directly represent relative humidity, the following formulation (ECMWF, 2016) was utilized to compute surface relative humidity (*hurs*) through dew point temperature (*tdm*) and surface air temperature (*tas*),

$$hurs = \frac{6.11 \times e^{\frac{17.67 \times tdm}{243.5 + tdm}}}{6.11 \times e^{\frac{17.67 \times tas}{243.5 + tas}}} \times 100. \quad (6)$$

Since the measured data did not cover the basin entirely, gridded reanalysis datasets were compared to the available stations for 1985–2005. To this end, statistical indices for different stations and variables were independently calculated and spatially averaged. Following Hemer and Trenham (2016), the indices were normalized so that the indices closer to zero showed the best performance. Error matrices for different coasts of the AS using normalized indices showed a better performance of ERA5 for surface temperature, relative humidity, surface pressure, and wind speed (Figures S4 and S5). This finding is valid for the stations on the north, west, and east coasts. However, for wind direction, ERAI outperforms the other datasets. A comparison of different reanalysis datasets and measured wind roses confirms the better performance of ERAI in terms of wind direction (Figures S4 and S5). Bearing in mind that due to the consistency of the climate variables, it is not reasonable to choose a different reference dataset for each climate variable. Hence, according to the overall performance of ERA5, this dataset was used as the reference for all the required climate variables.

2.3 | Climate models

The best-fitted reanalysis dataset was utilized as the reference to evaluate GCMs and form an ensemble to project the changes in the surface climate variables. Most GCMs consist of different ensembles due to different realizations, initializations, and physics of the models. The mean of all available ensembles was calculated for each climate model (see Table 3). Then, climate models and reference data were re-gridded onto a typical $1^\circ \times 1^\circ$ grid using bicubic interpolation methods applicable in CDO (Schulzweida,

TABLE 2 Reanalysis datasets information

Dataset	Temporal coverage	Spatial output resolution ($^\circ$)	Reference
ERA1	1979–2019	0.75 \times 0.75	Dee <i>et al.</i> (2011))
ERA5	1979–Present	0.5 \times 0.5	Hersbach <i>et al.</i> (2020))
NCEP/NCAR	1948–Present	2.5 \times 2.5	Kalnay <i>et al.</i> (1996))
CFSR	1979–2009	0.5 \times 0.5	Saha <i>et al.</i> (2010))

2019). The statistical indices (Equations (1)–(4)) were then utilized to rank GCMs according to their performances, where ref and sim refer to the reanalysis and GCM datasets, respectively. This was performed in the baseline period, starting from 1979 to 2005. The spatial average of statistical indices for the months with the highest

frequency of TCs, that is, May–June for spring and October–September for autumn, was subsequently calculated to compare model skills. Afterwards, the best GCMs were identified using a comprehensive rating index (CRI; Jiang *et al.*, 2015), which includes the performance of GCMs for all considered variables,

TABLE 3 CMIP5 models description

AGCMs	Model resolution	Historical period	Number of ensembles					Institution
			Historical	RCP2.6	RCP4.5	RCP6.0	RCP8.5	
ACCESS 1.0	1.25×1.875	1850–2005	1			1		Commonwealth Scientific and Industrial Research Organization (CSIRO) and Bureau of Meteorology (BOM), Australia
CMCC-CM	0.7484×0.75	1850–2005	1		1		1	Centro Euro-Mediterraneo per I Cambiamenti Climatici
CNRM-CM5-2	1.4008×1.40625	1850–2005	1	5	5		5	Centre National de Recherches Meteorologiques and Centre Europeen de Recherche et Formation Avancees en Calcul Scientifique
CSIRO-Mk3.6.0	1.8653×1.875	1850–2005	10	10	10	10	10	Queensland Climate Change Centre of Excellence and Commonwealth Scientific and Industrial Research Organisation
CanESM2	2.7906×2.8125	1850–2005	5	5	5		5	Canadian Centre for Climate Modelling and Analysis
FGOALS-s2	1.659×2.8125	1850–2005	3		3		3	The State Key Laboratory of Numerical Modeling for Atmospheric Sciences and Geophysical Fluid Dynamics, The Institute of Atmospheric Physics
GFDL-CM3	2×2.5	1860–2005	3	1	3	1	1	NOAA Geophysical Fluid Dynamics Laboratory
GFDL-ESM2M	2.0225×2.5	1861–2005	1	1	1	1	1	NOAA Geophysical Fluid Dynamics Laboratory
GISS-E2-H	2×2.5	1850–2005	1	1	5	1	1	NASA Goddard Institute for Space Studies
GISS-E2-H-CC	2×2.5	1850–2011	1		1		1	NASA Goddard Institute for Space Studies
HadGEM2-AO	1.25×1.875	1860–2005	1	1	1	1	1	National Institute of Meteorological Research/Korea Meteorological Administration
HadGEM2-ES	1.25×1.875	1860–2005	2	4	4	3	4	UK Met Office Hadley Centre
IPSL-CM5A-MR	1.2676×2.5	1850–2005	1	1	1	1	1	L'Institut Pierre-Simon Laplace Coupled Model
IPSL-CM5A-LR	1.8947×3.75	1850–2005	4	4	4	1	4	L'Institut Pierre-Simon Laplace Coupled Model
MIROC5	1.4008×1.40625	1850–2012	4	3	3	3	3	Atmosphere and Ocean Research Institute (The University of Tokyo), National Institute for Environmental Studies, and Japan Agency for Marine-Earth Science and Technology
MPI-ESM-MR	1.8653×1.875	1850–2005	2	1	3		1	Max Planck Institute Earth System Model
MPI-ESM-LR	1.8653×1.875	1850–2005	3	3	3		3	Max Planck Institute Earth System Model
MRI-CGCM3	1.12148×1.125	1850–2005	1	1	1	1	1	Meteorological Research Institute
NorESM1-M	1.8947×2.5	1850–2005	1	1	1	1	1	Norwegian Climate Centre
NorESM1-ME	1.8947×2.5	1850–2005	1	1	1	1	1	Norwegian Climate Centre

$$\text{CRI} = 1 - \frac{1}{m \times n} \sum_{i=0}^n \text{rank}_i. \quad (7)$$

In Equation (7), n is the number of variables, m is the number of GCMs, and rank addresses the rank of GCM for variable i , which was computed through statistical indices of Equations (1)–(4). Closer CRI values to 1 show better performance of the climate model.

Finally, an ensemble of the best performing GCMs was determined to compute the signals that alter the initial and boundary conditions of WRF model. It should be noted that the signals were first calculated for the best-performing GCMs individually by subtracting seasonal means of the baseline period from those of the future period. Then, the mean of the signals was calculated.

2.4 | Future tropical cyclones

2.4.1 | PGW simulations

Two tracks are typically associated with the TCs in the AS, that is, toward Oman coastlines (on the western parts of the basin) and Indian/Pakistan coastlines (on the eastern side). Cyclone Ashobaa is an example of a typical TCs that travels westward to make landfall in Oman (Figure 4). However, two cyclones known as Gonu and Phet are two exceptions in tracks; super cyclone Gonu made landfall in Iranian coastlines, and cyclone Phet made one landfall on the western coasts and travelled to the eastern coasts for its second landfall (Figure 4).

The WRF model has been utilized to simulate the historical TCs of Gonu, Phet, and Ashobaa in the AS (Soltanpour *et al.*, 2021). A summary of the model computational domain and configuration are presented in Tables 4

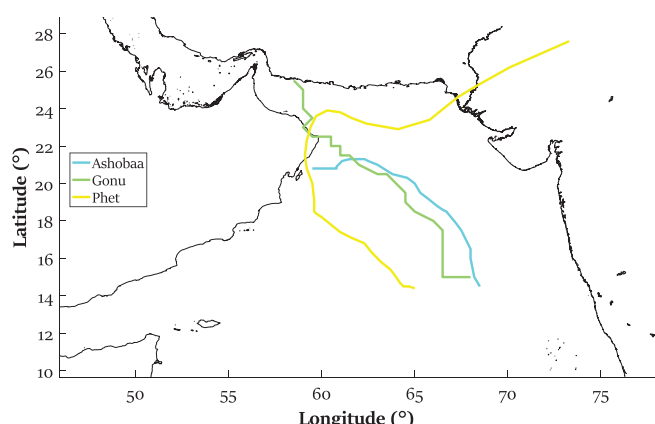


FIGURE 4 Tracks of cyclones Gonu (green), Phet (yellow), and Ashobaa (blue) [Colour figure can be viewed at wileyonlinelibrary.com]

and 5. Initial and boundary conditions were obtained from FNL and GFS global analysis datasets. GFS ANL is a 0.5° global analysis dataset. Similarly, FNL provides global analysis datasets in a 1° grid. However, FNL data is released 1 hr after GFS data to include more observational data. Horizontal and vertical resolutions of the computational domain were fixed for these three TCs. Cyclone Phet is better reproduced by moving nest option; however, cyclones Gonu and Ashobaa are reasonably well simulated with the fixed nest option. The results were sensitive to the start time and WRF physics. Thus, the best configuration was found through a trial-and-error process resulting in the best estimation of track and intensities of the TCs.

Here, the PGW approach was applied to project the future patterns of the aforementioned TCs in the AS, using the best ensemble of GCMs. To this end, the June signals for different variables, that is, air temperature, relative humidity, zonal and meridional wind speeds, geopotential height, surface pressure, and sea surface temperature, were interpolated to WRF model domains. They were then spatially added to the initial and boundary conditions of the calibrated model for the baseline period.

2.4.2 | PGW uncertainties

Since the WRF model, to a large extent, is sensitive to initial and boundary conditions, some of the sources of uncertainties that considerably influence the future projection of TCs are investigated here. These uncertainties have not been addressed systematically in most previous PGW studies. These can be categorized into selection of GCMs and climate variables, and spatial variation of signals that were addressed in the following subsections. Altogether 16 different initial and boundary conditions were reproduced, as depicted in Figure 5. All the simulations were conducted for the far-future period under RCP8.5.

3 | RESULTS AND DISCUSSIONS

3.1 | Climate models (baseline period)

3.1.1 | Evaluation of intermodel variability

To investigate intermodel variability, linear trends of yearly averaged variables were computed for both GCMs and reference data. Calculated trends were normalized by the trend of the reference data to show the variability of different variables. All GCMs trends were first evaluated based on p -value, which offers a 95% level of significance against the null hypothesis. Analysing the box plots of the trends for GCMs, the most significant difference

TABLE 4 Details of temporal and spatial features of WRF model (Soltanpour *et al.*, 2021)

Model component	Ashobaa 2015	Phet 2010	Gonu 2007
Model version	3.9.1		
Start time	June 6th, 0000 UTC	June 1th, 0000 UTC	June 2nd, 0000 UTC
Initial and boundary conditions	FNL (1°)	FNL (1°)	GFS ANL (0.5°)
Nesting type	Fixed nest	Moving nest (vortex following)	Fixed nest
Vertical resolution	40 terrain-following sigma mass coordinate		
Horizontal resolution and domains	30 km: 62.5 E–17.5 N (210 × 180) 10 km: 58.31 E–19.03 N (517 × 277)		

TABLE 5 Selected physics schemes for TCs simulation (Soltanpour *et al.*, 2021)

TCs	Microphysics scheme	Cumulus scheme	Land surface scheme	Surface layer scheme	Shortwave and longwave radiation schemes	PBL scheme
Ashobaa 2015	WSM3 (Hong <i>et al.</i> , 2004)	Grell 3D Ensemble (Grell, 1993; Grell and Dévényi, 2002)	Unified Noah Land Surface (Tewari <i>et al.</i> , 2004)	Revised MM5 Scheme (Jiménez <i>et al.</i> , 2012)	Dudhia and RRTM (Dudhia, 1989; Mlawer <i>et al.</i> , 1997)	YSU (Hong <i>et al.</i> , 2006)
Phet 2010	Thompson (Thompson <i>et al.</i> , 2008)	Grell–Freitas Ensemble (Grell and Freitas, 2014)	5-layer Thermal Diffusion (Dudhia, 1996)		RRTMG (Iacono <i>et al.</i> , 2008)	
Gonu 2007	WSM6 (Hong and Lim, 2006)	Kain–Fritsch (Kain, 2004)			Dudhia and RRTM (Dudhia, 1989; Mlawer <i>et al.</i> , 1997)	

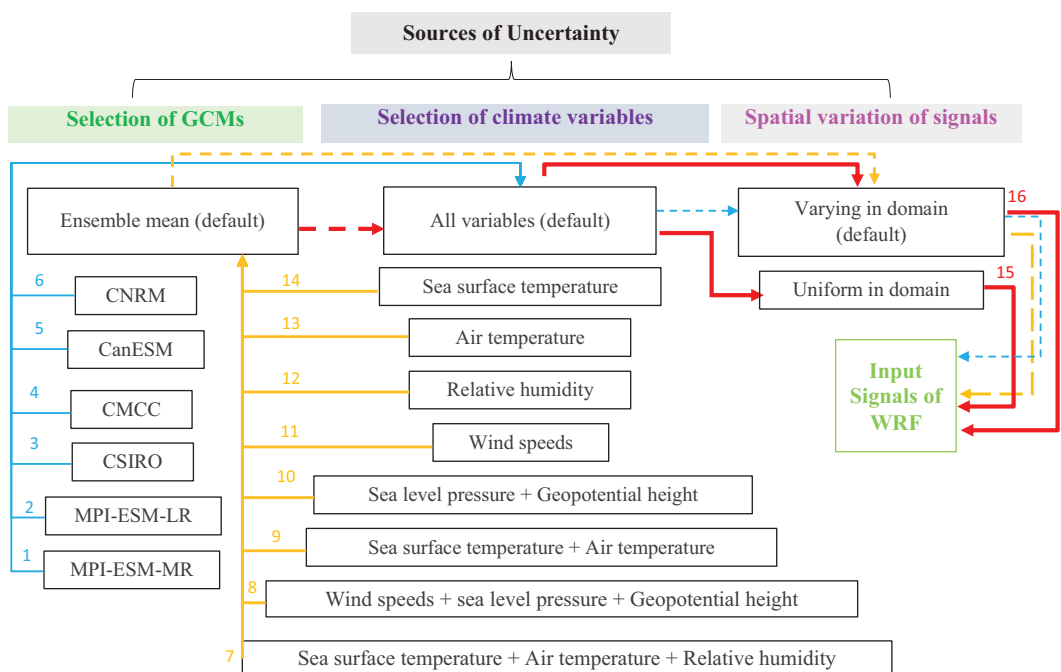


FIGURE 5 Uncertainties in computing the signals used for changing the initial and boundary conditions of WRF model. The paths 1–6 for the uncertainty of GCMs (blue), 7–14 for the uncertainty of climate variables (orange), and 15–16 for the uncertainty of spatial variation of the signals (red). Solid lines denote each simulation, while dashed lines point to the connection of each section to the others. By following each number with the arrows whose colour is as same the number, the configuration of each simulation can be recognized (see also Figure S13 and Tables S1 and S2) [Colour figure can be viewed at wileyonlinelibrary.com]

between GCM trends was observed for wind speed. Minimum intermodel variability was found for the trend of sea level pressure. Relative humidity showed a positive trend in GCMs, while a negative trend was observed for reanalysis data. The yearly averaged trend was positive (negative) for surface air temperature and wind speed (sea level pressure) in GCMs, which are in agreement with the trend of the reference data (Figures S6–S9).

3.1.2 | Evaluation of spatial variability

Taylor diagrams (Taylor, 2001) are employed to evaluate the performance of GCMs to project spatial patterns of the considered variables (Figure 6). In this regard, the averaged variables for the baseline period, for each grid of GCMs and reference data, were computed, and the results were then compared. Compared to other variables, wind speed of GCMs showed the lowest difference from that of the reference data (correlation coefficients ranging from 0.8 to 0.95). Moreover, GCMs had a closer SD to the reference data for wind speed. Higher similarity to wind speeds of the reference data is presented by CSIRO and CNRM, while the least similarity to reference data is observed in NorESMs.

A wider range of correlation coefficients, that is, 0.2–0.95, was found for sea level pressure. MRI showed poor

performance against reference data, but CNRM and CSIRO present the best agreement.

All GCMs had a larger SD than the reference data for relative humidity with a limited correlation coefficient range, that is, 0.7–0.8. CNRM and CanESM showed better agreements with reference data.

A significant difference between GCMs and reference data was observed in surface air temperature correlation coefficients (i.e., 50–90%). CNRM and MIROC present the highest and lowest similarity to the reference data, respectively.

In general, GCMs with a higher resolution (e.g., MRI), compared to lower resolution (e.g., CNRM), do not show promising agreement with reference data. This issue implies the lower importance of model resolution for reproducing climate variables by GCMs. Therefore, considering the spatial resolution of GCMs as the only criterion to select GCMs is not a reliable approach.

3.1.3 | Evaluation of temporal variability

Since the maximum frequency of TCs occurs during specific periods (Figure 3), that is, May–June and October–September, the performance of GCMs needs to be validated within the periods. This was carried out by

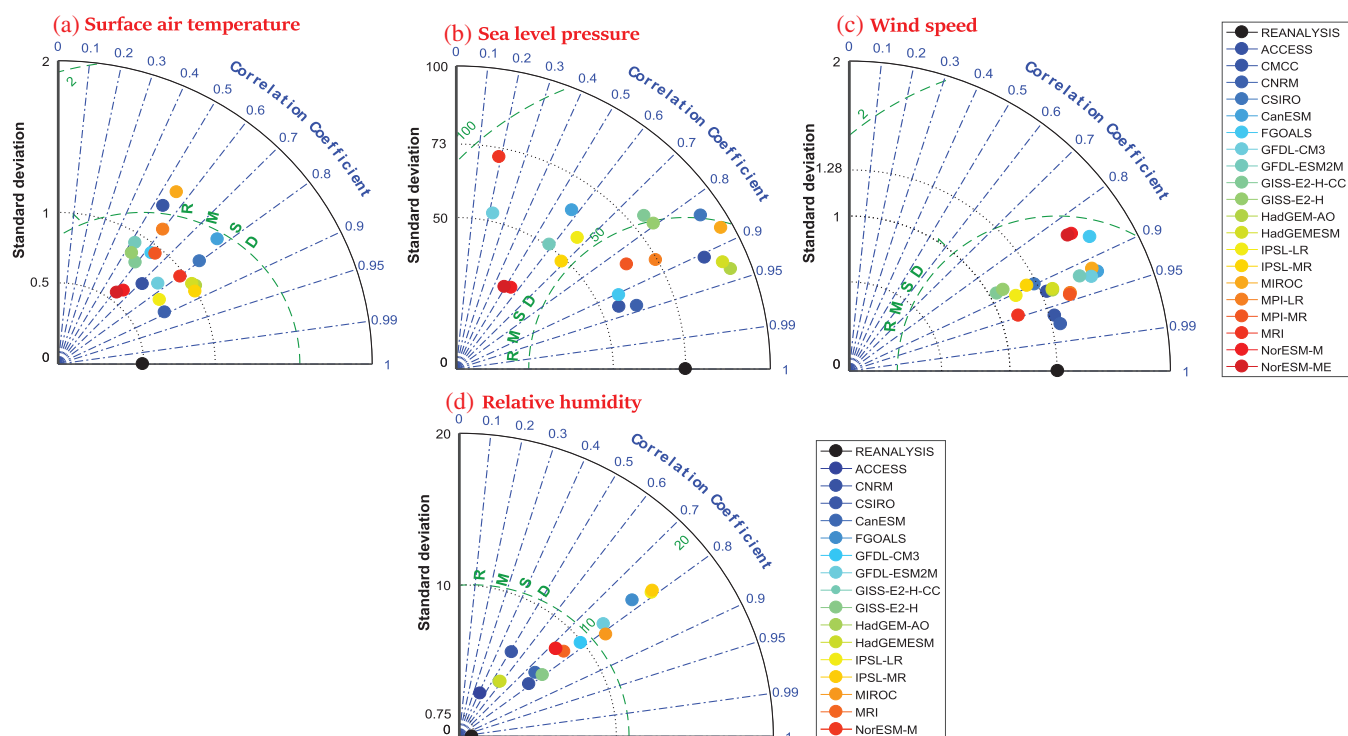


FIGURE 6 Taylor diagrams for spatial averaged variables of (a) surface temperature, (b) surface pressure, (c) relative humidity, and (d) wind speed in the baseline period [Colour figure can be viewed at wileyonlinelibrary.com]

considering the average of statistical indices in May–June as the spring season and October–September as the autumn season. Thereafter, all averaged indices were normalized to a unique measure with zero for the best and one for the worst model performance. Error matrices are presented for different variables, statistical indices, and seasons. Since not all GCMs simulate relative humidity (i.e., CMCC and MPIs), error matrices for this variable are shown for the rest of the GCMs, separately (see Figures S6–S9).

Considering the error matrices, the best GCMs to reproduce sea level pressure are CNRM, FGOALS, and MPI-LR in spring, while GISSs show better performance for autumn. CNRM and CanESM fairly simulate surface air temperature in spring. For autumn, top-ranked GCMs are CNRM and ACCESS. CMCC, CNRM, and GFDL-ESM2M represent the best-simulated wind speed in spring, while for autumn, CNRM, IPSL-LR, and GFDL-ESM2M are the GCMs with the highest performance. CSIRO, HadGEMESM, MPI-MR, and CNRM exhibit the lowest wind direction difference with reference data in spring. In autumn, MPI-MR, HadGEM-AO, and GFDL-CM3 demonstrate better performance in the simulation of wind direction. The relative humidity reproduced by CSIRO, and CanESM adequately fits with reference data.

The overall GCM performance for all variables was evaluated using CRI, and a multimodel ensemble was created accordingly. The ranks of GCMs, according to the CRI criterion, are represented in Figure 7. Generally, among the 20 GCMs listed in Table 3, CNRM better reproduces all climate variables in both seasons. An ensemble including CNRM, CMCC, CanESM, CSIRO, and MPIs is recommended for future projection of the

variables in spring. The autumn ensemble is created by CNRM, IPSL-MR, CanESM, and MPI-MR.

To gain more insight into the performance of the proposed ensembles of the GCMs, the seasonal mean of each variable obtained from the ensemble mean and top-ranked GCMs were compared with that of reference data (see Figures S6–S9). In spring, all variables were better reproduced by the mean of the ensemble. In particular, the spatial pattern is similar to that of the reference data. However, the differences with reference data are considerable for relative humidity and surface air temperature, either in the mean of the ensemble or top-ranked GCMs. Similar behaviour was observed in autumn, except for sea level pressure and wind direction, which are better represented by top-ranked GCMs.

3.2 | Climate models (near and far future periods)

Compared to the reference data, the biases for baseline and future periods could also be corrected. Since the bias correction methods (e.g., delta scaling) modify climate variables for both baseline and future periods and do not change the variables' signals and trends remarkably (see Figure S10 for details), it can be assumed that the bias correction is not essential for the PGW approach used in this study. Moreover, applying correction factors that do not change with time cannot correct the errors of the climate variables in the regions with strong intra-annual and interannual variability, for example, the AS (Lemos *et al.*, 2020).

The spatial patterns of the averaged signals in springs and autumns of the near future and far future are

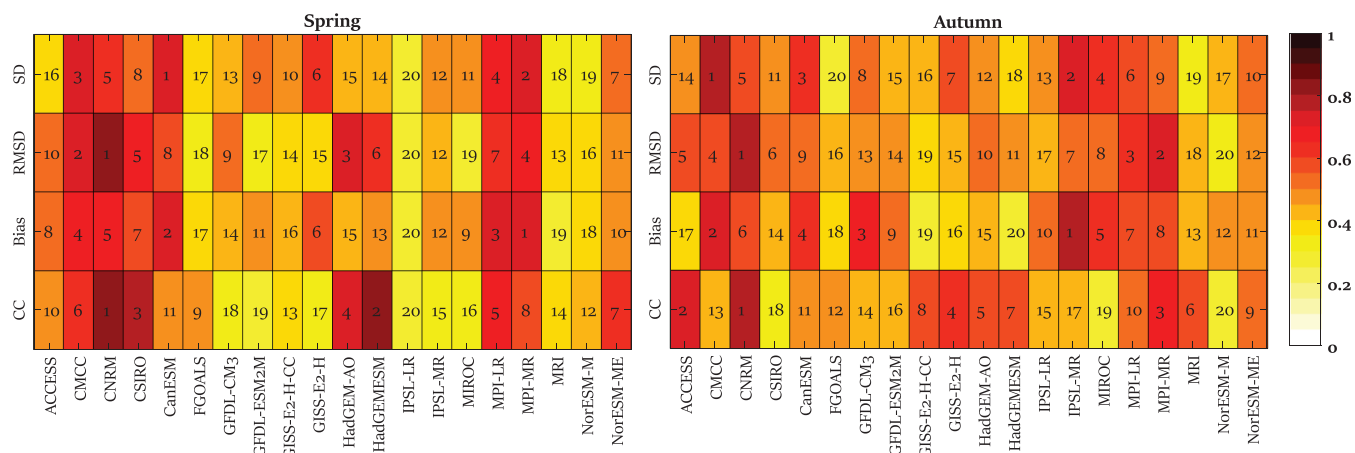


FIGURE 7 Error matrix for computed CRI in (left) spring and (right) autumn [Colour figure can be viewed at wileyonlinelibrary.com]

illustrated in Figures 8 and 9. They show insignificant differences between the signals of RCP4.5 and RCP8.5 in the near future. However, these differences become considerable for longer timespans. Relative humidity will increase in coastal areas and decrease in deeper waters during the future spring season. A 20% decrease in relative humidity during the future autumn season occurs in higher latitudes of the AS. A higher increase in surface air temperature is observed during the future spring of the northern coastlines and future autumn of the eastern parts of the AS. Sea level pressure increases by 30 Pa in the eastern sides for the future spring. This increase, on the other hand, is considerable in the northern sides for future autumn. In the western coastlines, wind speed will increase by 1 and 10 $\text{m}\cdot\text{s}^{-1}$ for future spring and autumn, respectively. In general, wind direction changes around 200° during future spring, while the changes are insignificant during future autumn, except in the southwestern parts of the basin.

3.3 | Future tropical cyclones

3.3.1 | PGW simulations

Vertical profiles of horizontally averaged signals over the WRF domain for relative humidity, air temperature, zonal and meridional wind speeds, and geopotential height reveal that maximum signals of all variables are projected around 100–200 hPa (Figures S11 and S12). Although the vertical profiles for the near future under different RCPs are almost similar, for the far future under RCP8.5, radical changes in vertical profiles were observed. For the surface level, minor changes of the climate variables are found, excluding meridional winds and temperature. A considerable decrease of signals also appears for these two variables around the surface level. Air temperature tends to decrease at the highest levels, while for the other variables, the top-level changes are

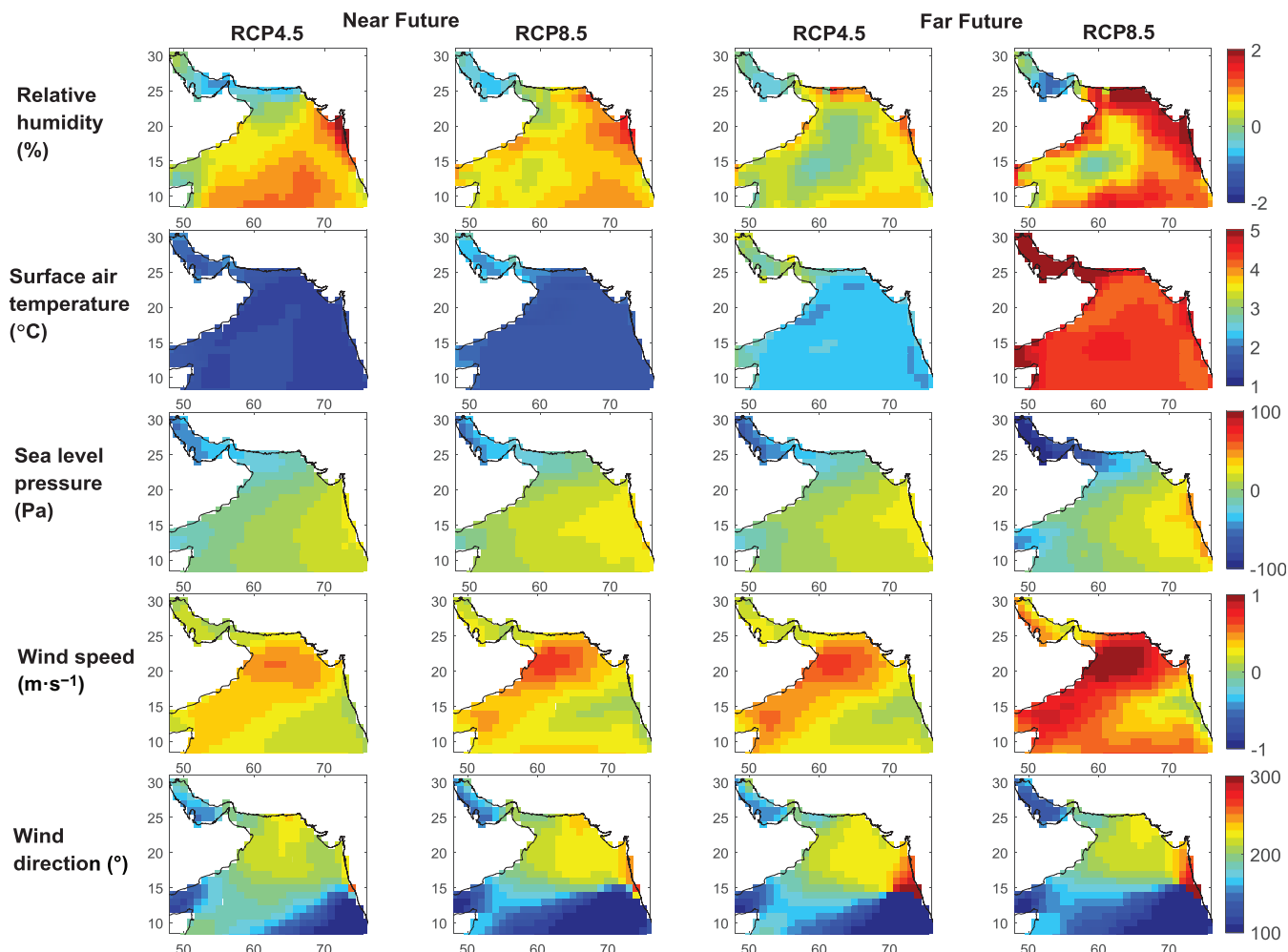


FIGURE 8 Spatial patterns of the ensemble mean of signals for relative humidity, surface air temperature, sea level pressure, wind speed, and wind direction in (left) near future and right) far-future spring over the AS; the signals are obtained from the difference of the seasonal means of the future with those of the baseline [Colour figure can be viewed at wileyonlinelibrary.com]

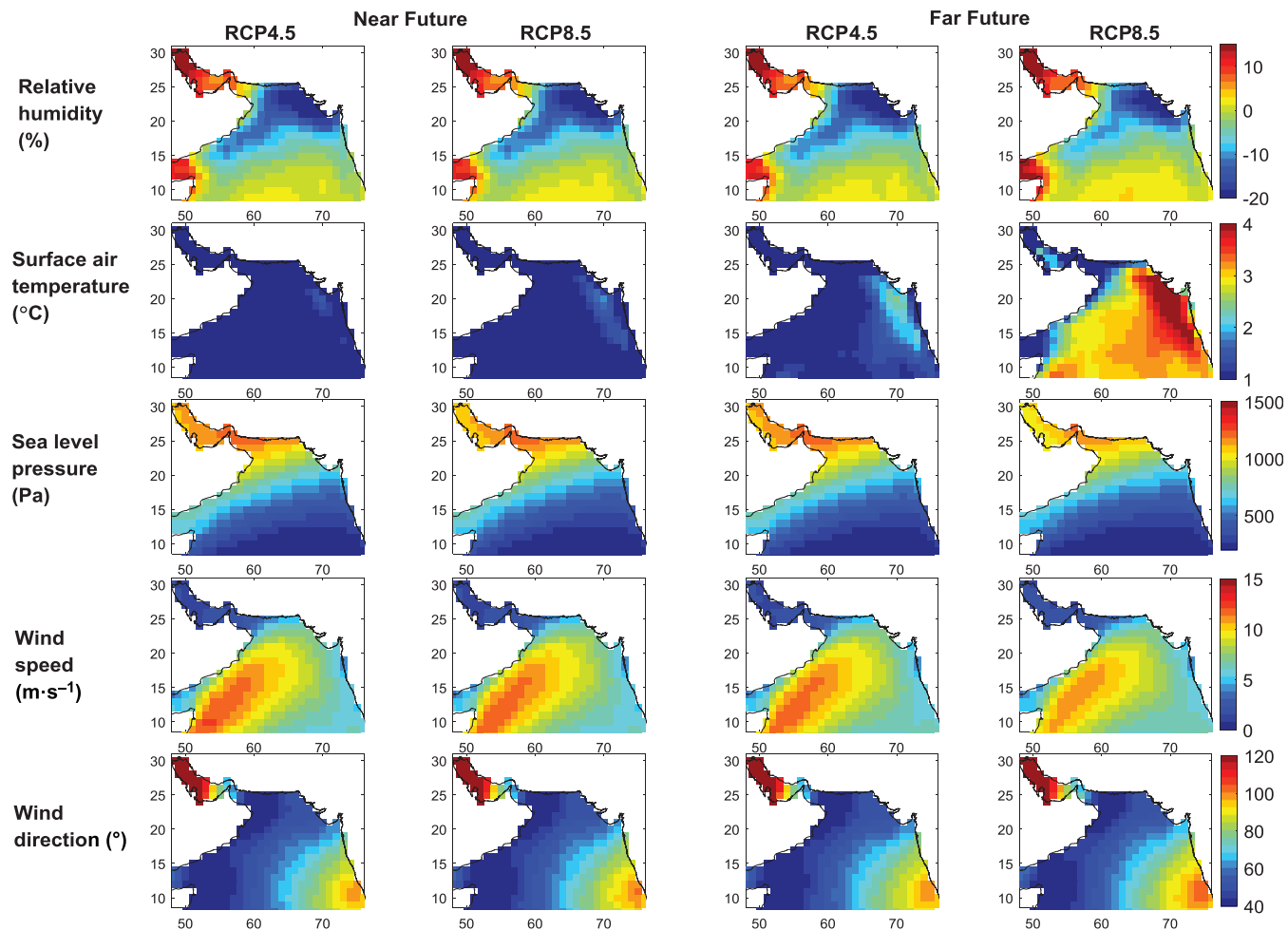


FIGURE 9 Spatial patterns of the mean ensemble of signals for relative humidity, surface air temperature, sea level pressure, wind speed, and wind direction in (left) near future and (right) far-future autumn over the AS; the signals are obtained from the difference of the seasonal means of the future with those of the baseline [Colour figure can be viewed at wileyonlinelibrary.com]

approximately zero. Meridional wind speed shows a maximum decrease of $0.5 \text{ m}\cdot\text{s}^{-1}$ around 300 hPa that eventually increases to a maximum signal of $0.6 \text{ m}\cdot\text{s}^{-1}$ near 100 hPa.

The spatial pattern of the sea surface temperature signal (Figures S11 and S12) indicates that the western coasts of the AS face a lower increase in temperature. Thus, the tracks of typical westward TCs are likely to change. This is established by future simulations of cyclones Gonu and Ashobaa, which made landfall on the western coasts. As a result, the future TC tracks were shifted toward the east (see Figure S13 and Tables S1 and S2). Cyclone Phet also moved farther than its first landfall on the west coasts, but it kept moving to the eastern coastline. For further comparison of the TC intensity in different climates, more or less similar TC tracks in the present and future climates were required. Thus, we only considered cyclone Phet to estimate the future projection of TCs in the AS. It also showed that the cyclones with

westward tracks were more likely to recurve eastward in future June.

We first evaluated the track and intensity of cyclone Phet for the near future and far future under RCP4.5 and RCP8.5 (see Figure 10). Almost all WRF simulations show similar tracks. However, a simulation associated with far future forcing, under RCP8.5, leads to a significant shift in the track of cyclone Phet. It should be noted that this shift is negligible in the initial time when it becomes the most intense TCs compared to the other cases. Comparing the simulated cyclones for near future under RCP4.5 and 8.5, it can be concluded that the TCs is not necessarily intensified under the worst emission scenario (RCP8.5). It is due to the negligible differences between the variables' signals of RCP4.5 and RCP8.5 in the near future (Figure 8). However, more intense TCs are likely to generate in the far future compared to the near future. In general, cyclone Phet shows an intensification of 10–15% in the future climate. One may

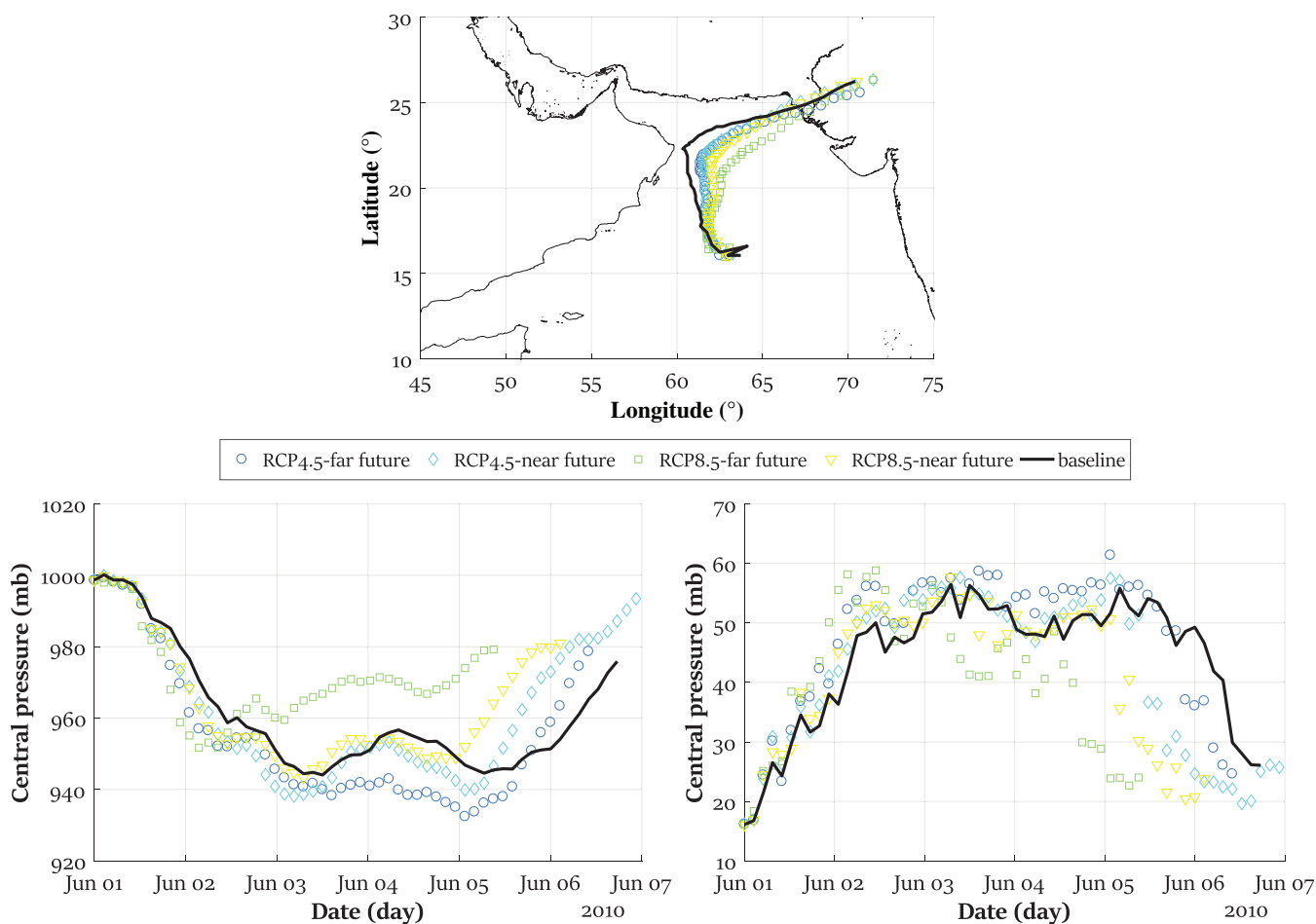


FIGURE 10 Simulated tracks (top) and intensities (bottom) of cyclone Phet for present climate (solid line), the future climate in RCP4.5 (circles and diamonds), and in RCP8.5 (rectangular and triangular) [Colour figure can be viewed at wileyonlinelibrary.com]

consider this intensification cautiously, as it includes several uncertainties that are discussed in the next section.

3.3.2 | PGW uncertainties

GCMs contribution to the input signals

In the PGW approach, the input signals are computed by climate models, which are either randomly selected or represented by an ensemble mean. To indicate the necessity of evaluating GCMs before the computation of the signals, we presented future TCs using individual and the mean ensemble of top-ranked GCMs. Figure 11 shows large differences between future projections of the TC track with the input signals computed by different GCMs. The CSIRO and CNRM have the maximum and minimum track shifts, respectively. The track shift resulting from the ensemble mean is also significant, compared to those of CNRM, CanESM, and MPI-ESM-MR models. Figure 11 illustrates that the most intensified Phet is

attributed to the GCMs with lower shifts from the tracks of the baseline simulations. It reveals that the selection of the ensemble members contributing to the computation of the input signals remarkably affects the characteristics of the future TCs.

Input signals variables

Nine different sets of variables (see Figure 5, paths of 7 to 14) were considered to apply future signals to the initial and boundary condition of WRF model. Future simulations of cyclone Phet are depicted in Figure 12. All cases, excluding SST and AT, have similar landfall locations. SST and AT reveal different intensities, according to the different tracks and points of landfall, which are maximum and minimum intensities, respectively. Comparison of the results of two cases that include all variables and AT-SST signals shows that the most effective climate variables on the future TC characteristics are air temperature and sea surface temperature (Figure 12). The rest of the variables barely change TC track and intensity.

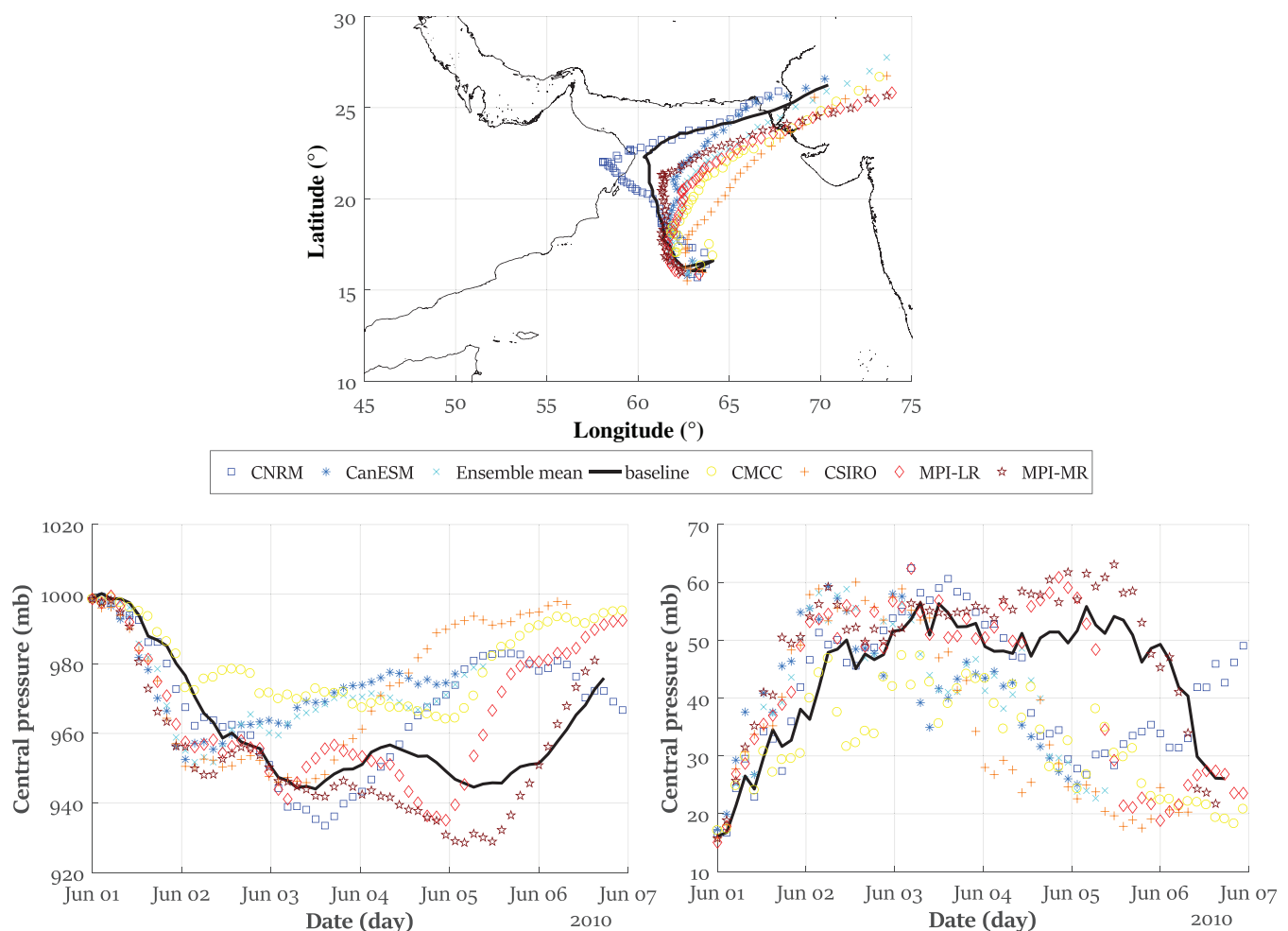


FIGURE 11 Simulated tracks (top) and intensities (bottom) of cyclone Phet for present climate (black) and the future climate in RCP8.5 for the ensemble mean and top-ranked individual GCMs [Colour figure can be viewed at wileyonlinelibrary.com]

Spatial variation of signals

Two different approaches were utilized to apply the computed signals to the initial and boundary conditions of WRF model. The signals were first averaged over the computational domain. Then, the average values were added as constants to each vertical level of WRF inputs. As mentioned before, more recently, instead of considering constant signals in time and space, spatially and temporally varying signals are also accounted for. Here, the changes in the future projection of TCs caused by the spatial variability of the input signals was also examined. Figure 13 shows a significant shift of the TC track by assuming constant input signals. This shift is still considerable for spatially varying signals, but is closer to the simulated track in the baseline. Due to the shifts in tracks, the intensities cannot be compared directly.

4 | LIMITATIONS AND THE WAY FORWARD

The PGW approach, in its nature, includes some limitations that can lead to the unrealistic future projection of TCs. On top of that, the superposition of historical climate variables and long-term signals might be nonphysical. In the PGW approach, only limited numbers of climate variables are considered for the future projections.

Apart from the limitations of the PGW approach, there are other sources of errors that should be addressed through uncertainty analysis. To address the uncertainties in the projection of future patterns of TCs for the study area, a limited number of simulations (i.e., 16 cases as the minimum required numbers of simulations) among all possible selections of best performing GCMs, climate variable sets, and spatial variation of variables

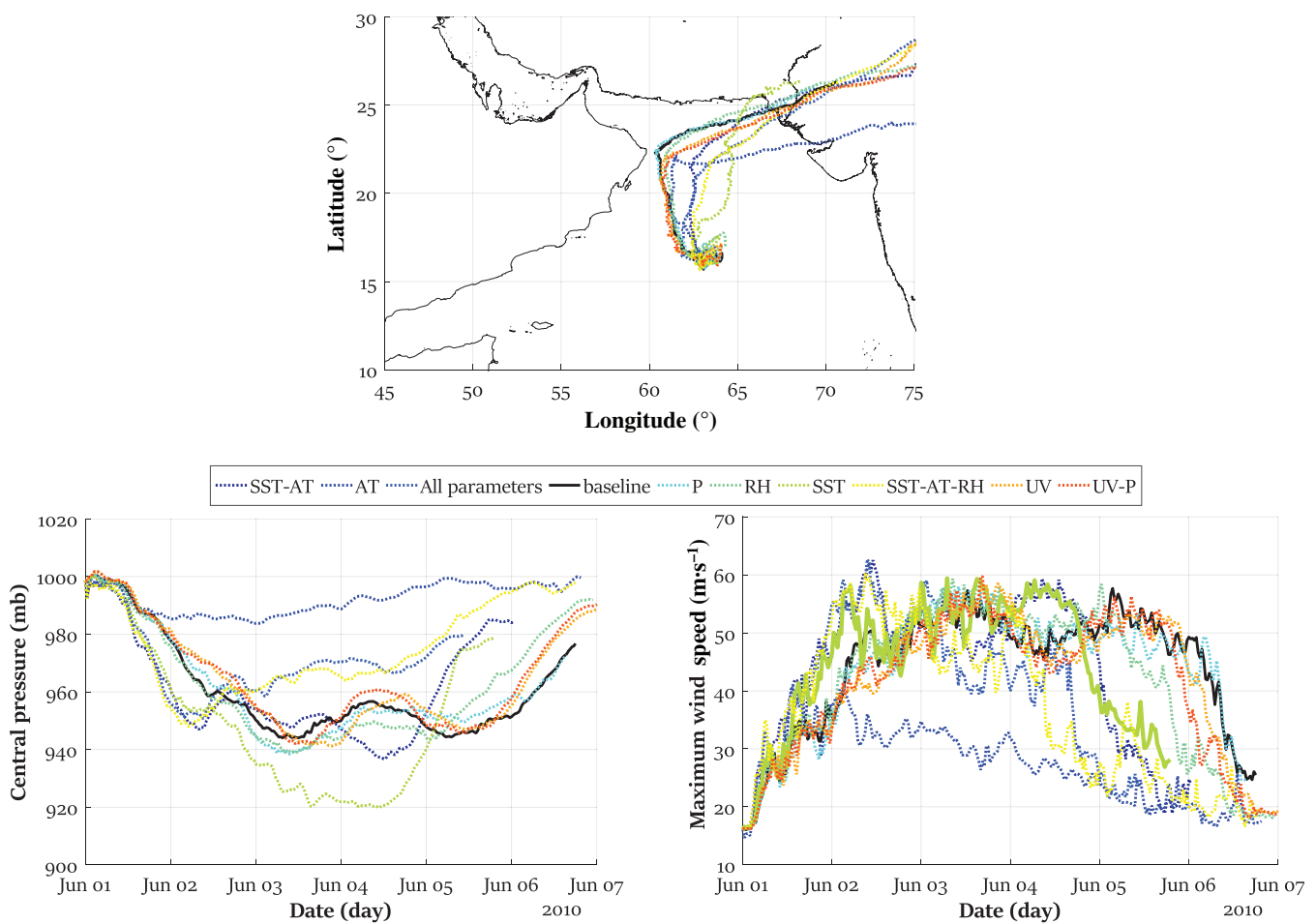


FIGURE 12 Simulated tracks (top) and intensities (bottom) of cyclone Phet for present climate (black), the future climate in RCP8.5 by including different climate variables. AT, SST, P, RH, UV denote air temperature, sea surface temperature, sea level pressure, and geopotential height, relative humidity, and wind speeds, respectively [Colour figure can be viewed at wileyonlinelibrary.com]

(in aggregate 126 cases) were considered. In this way, the high computational costs of WRF simulations were reduced to get an overview of CC impacts on TCs and the associated uncertainties. However, even by increasing the number of simulations, the PGW approach is not applicable to the TC, whose track shifts significantly from the corresponding baseline track. It should also be noted that by considering only three cyclones, we cannot present a precise projection for future TCs. To this end, additional TCs, together with additional sets of physical schemes should be further investigated. Increasing the number of simulations and adding GCMs from the CMIP6 while considering the aforementioned limitation of PGW is the way forward to this research.

A large number of factors (e.g., physics schemes, initial conditions) control the performance of the WRF model. A sensitivity analysis was performed for each TC in the baseline period (Soltanpour *et al.*, 2021), which shows that these sources change the TC track and intensities remarkably. For example, changing the microphysics shifts the

track and reduces the intensification by 5% for cyclone Gonu. Thus, these sources need to be quantified as an additional part of uncertainty analysis. Semiprobabilistic modelling (i.e., ensemble modelling) and ranking uncertainty sources are the future works of this paper's authors.

5 | SUMMARY AND CONCLUSIONS

Different approaches have been used to study the future changes of TCs, among which PGW utilizes signals of the climate variables. In this approach, by adding the signals to the initial and boundary conditions of the atmospheric models, the future variations of the historical TCs can be projected. These signals are accessible through the available GCMs. Using different GCMs or an ensemble of them as the forcing conditions can significantly influence the TC projections. Hence, it is essential to validate their performance in the study area before utilizing them. This

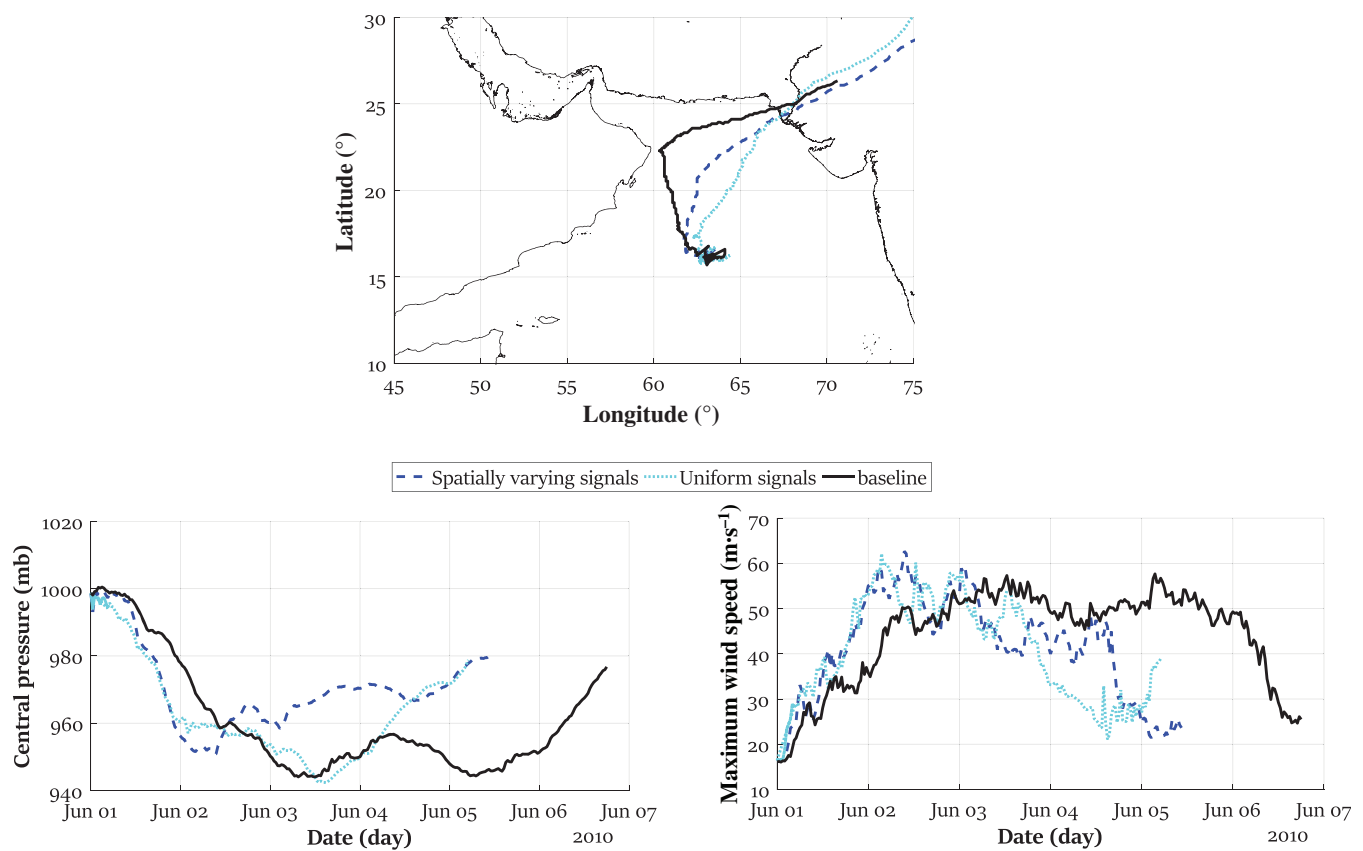


FIGURE 13 Simulated tracks (top) and intensities (bottom) of cyclone Phet for present climate (solid line), the future climate in RCP8.5 with spatially varying (dashed line) and constant (dotted line) signals in the domain [Colour figure can be viewed at wileyonlinelibrary.com]

issue was generally overlooked in most of the previous research. To address the importance of GCMs evaluation, an intercomparison of 20 GCMs of CMIP5 is included in this study, leading to the selection of best performing GCMs to project the future climate variables. For this purpose, we first validated available reanalysis datasets against the available long-term measurements of the climate variables affecting the patterns of TCs. It was found that ERA5 better reproduces the variables of surface air temperature, sea level pressure, relative humidity, and wind speed. As a result, ERA5 was selected as the reference data for further evaluation of the GCMs performance. Then, two temporal periods with more frequent TCs (i.e., May–June as spring and October–September as autumn) were chosen to validate GCMs against the reference data. To this end, several comparisons (e.g., Taylor diagrams and error matrices) were made to create an ensemble of the most compatible GCMs to estimate the future projection of climate variables.

CNRM, CMCC, CanESM, CSIRO, and MPIs were selected as the ensemble members to project the changes in climate variables during the spring season. The autumn ensemble was created by CNRM, IPSL-MR, CanESM, and MPI-MR. Except for relative humidity, all

variables presented by the mean of ensembles were in reasonable agreement with those of the reference data.

As the GCM data for the baseline period had some biases compared to the reference data, the biases were also corrected. Nonetheless, after implementing several bias correction methods, it was found that the correction has no considerable effects on the computed signals. Thus, the bias correction was omitted from the process of signals' computations.

The future patterns of three different historical tropical cyclones of Gonu, Phet, and Ashobaa were projected using the PGW approach. For this purpose, signals of climate variables were first computed for the top-ranked GCMs and then averaged to create an ensemble mean for the middle and the end of the century under RCPs 4.5 and 8.5. Since the projected tracks of Gonu and Ashobaa are quite different from their simulated tracks in the present climate, only cyclone Phet was considered for further investigation. The tendency of Gonu and Ashobaa to make landfall on the northeast of the AS agrees with findings of Murakami *et al.* (2017), which showed a higher concentration of track to the northeastward AS, in future springs, that is, a higher number of TCs that will travel or make landfall in this region. Future projections

of cyclone Phet for different emission scenarios in the mid and far future shows a rough intensification of 10–15%. However, according to the limitations of this research and uncertainties of the PGW approach, as discussed before, this intensification should be taken with a lot of caution. To investigate the reliability of the PGW approach, additional simulations were also conducted. The sources of uncertainty (i.e., GCMs, climate variables, the spatial variations of the signals) that effectively change the future projection of TCs were addressed by 16 different simulations. To the knowledge of the authors, these sources were not addressed systematically in previous PGW studies. The additional simulations were conducted for only one cyclone (i.e., Phet), under only one emission scenario (i.e., RCP8.5).

By introducing the signals obtained from different GCMs to the PGW approach, different tracks and intensities for cyclone Phet under RCP8.5 were projected, implying the necessity of evaluating GCMs before computing the signals.

Given different sets of climate variables to extract the signals, it was found that sea surface temperature and air temperature have major effects on cyclone Phet's track and intensity, among other variables. According to this finding, the shifts in the tracks of Gonu and Ashobaa were also likely affected by the remarkable increase of sea surface temperature and air temperature near the eastern coastlines. These changes in tracks and intensities of TCs in a warmer environment were previously shown by Katsube and Inatsu (2016). They found out that TCs in the warm climate, as a result of the SST increase, tended to move northward rapidly, regardless of their original tracks. It was also noted that the warmer upper ocean is a favourable environment for TCs to sustain or increase their intensity. This is mainly due to the sensible and latent heat fluxes supplied from the ocean surface to the atmosphere (Rajeevan *et al.*, 2013).

Different tracks were also observed by applying different spatial variations for the signals of climate variables. So, the way by which the signals are applied to the initial and boundary conditions of the WRF is also crucial for the projection of TCs.

Considering these 16 simulations, it was also concluded that the uncertainties changing the TC tracks have a lower impact on the maximum wind speed, compared to the central pressure. This was partially described by the findings of Chavas *et al.* (2017), who showed that the central pressure is an intensity measure that combines maximum wind speed, storm size, and background rotation rate. Therefore, by changing the TC characteristics in different simulations, central pressure and maximum wind speeds, as measures of TC intensity, can change differently. Here, it was found that central

pressure is more sensitive to the uncertainties associated with PGW approach.

Although some uncertainties associated with the PGW approach were addressed in this study, there are still other sources (e.g., using more GCMs, considering WRF model uncertainty) that need to be accounted for in future works.

A MATLAB software package by the authors for the intercomparison of GCMs and future projection of climate variables can be found at <https://github.com/zranji/Toolbox-for-analyzing-and-visualizing-the-outputs-of-global-climate-models>.

ACKNOWLEDGEMENTS

The authors would like to thank Dr. A. Izadi and Dr. S. Moradian from K. N. Toosi University of Technology and Dr. R. Nakamora from Niigata University for their kind technical assistance.

AUTHOR CONTRIBUTIONS

Zahra Ranji: Conceptualization; data curation; formal analysis; methodology; software; validation; visualization; writing – original draft. **Amin Reza Zarifsanayei:** Conceptualization; formal analysis; methodology; resources; validation; writing – review and editing. **Nick Cartwright:** Conceptualization; methodology; writing – review and editing. **Mohsen Soltanpour:** Conceptualization; methodology.

ORCID

Zahra Ranji  <https://orcid.org/0000-0003-0718-6058>

REFERENCES

- Balaji, M., Chakraborty, A. and Mandal, M. (2018) Changes in tropical cyclone activity in north Indian Ocean during satellite era (1981–2014). *International Journal of Climatology*, 38(6), 2819–2837. <https://doi.org/10.1002/joc.5463>.
- Bell, S.S., Chand, S.S., Tory, K.J., Ye, H. and Turville, C. (2020) North Indian Ocean tropical cyclone activity in CMIP5 experiments: future projections using a model-independent detection and tracking scheme. *International Journal of Climatology*, 40(15), 6492–6505. <https://doi.org/10.1002/joc.6594>.
- Chavas, D.R., Reed, K.A. and Knaff, J.A. (2017) Physical understanding of the tropical cyclone wind-pressure relationship. *Nature Communications*, 8(1), 1360. <https://doi.org/10.1038/s41467-017-01546-9>.
- Chen, J., Wang, Z., Tam, C.Y., Lau, N.C., Lau, D.S.D. and Mok, H. Y. (2020) Impacts of climate change on tropical cyclones and induced storm surges in the Pearl River Delta region using pseudo-global-warming method. *Scientific Reports*, 10(1), 1–10. <https://doi.org/10.1038/s41598-020-58824-8>.
- Cordero, E.C., Kessomkiat, W., Abatzoglou, J. and Mauget, S.A. (2011) The identification of distinct patterns in California temperature trends. *Climatic Change*, 108(1), 357–382. <https://doi.org/10.1007/s10584-011-0023-y>.

- Dee, D.P., Uppala, S.M., Simmons, A.J., Berrisford, P., Poli, P., Kobayashi, S., Andrae, U., Balmaseda, M.A., Balsamo, G., Bauer, P., Bechtold, P., Beljaars, A.C.M., van de Berg, L., Bidlot, J., Bormann, N., Delsol, C., Dragani, R., Fuentes, M., Geer, A.J., Haimberger, L., Healy, S.B., Hersbach, H., Hölm, E. V., Isaksen, L., Källberg, P., Köhler, M., Matricardi, M., McNally, A.P., Monge-Sanz, B.M., Morcrette, J.-J., Park, B.-K., Peubey, C., de Rosnay, P., Tavolato, C., Thépaut, J.-N. and Vitart, F. (2011) The ERA-Interim reanalysis: configuration and performance of the data assimilation system. *Quarterly Journal of the Royal Meteorological Society*, 137(656), 553–597. <https://doi.org/10.1002/qj.828>.
- Deshpande, M., Singh, V.K., Ganadhi, M.K., Roxy, M.K., Emmanuel, R. and Kumar, U. (2021) Changing status of tropical cyclones over the north Indian Ocean. *Climate Dynamics*, 57, 3545–3567. <https://doi.org/10.1007/s00382-021-05880-z>.
- Dudhia, J. (1989) Numerical study of convection observed during the winter monsoon experiment using a mesoscale two-dimensional model. *Journal of the Atmospheric Sciences*, 46(20), 3077–3107. [https://doi.org/10.1175/1520-0469\(1989\)046<3077: NSOCOD>2.0.CO;2](https://doi.org/10.1175/1520-0469(1989)046<3077: NSOCOD>2.0.CO;2).
- Dudhia, J. (1996) A multi-layer soil temperature model for MM5. In: *Sixth PSU/NCAR Mesoscale Model Users' Workshop*. Boulder, CO: NCAR, pp. 49–50.
- ECMWF. (2016) *IFS documentation—Cy31rl, Part IV: Physical processes*. Reading: ECMWF.
- Evan, A.T. and Camargo, S.J. (2011) A climatology of Arabian Sea cyclonic storms. *Journal of Climate*, 24(1), 140–158. <https://doi.org/10.1175/2010JCLI3611.1>.
- Grell, G.A. (1993) Prognostic evaluation of assumptions used by cumulus parameterizations. *Monthly Weather Review*, 121(3), 764–787. [https://doi.org/10.1175/1520-0493\(1993\)121<0764:PEOAUB>2.0.CO;2](https://doi.org/10.1175/1520-0493(1993)121<0764:PEOAUB>2.0.CO;2).
- Grell, G.A. and Dévényi, D. (2002) A generalized approach to parameterizing convection combining ensemble and data assimilation techniques. *Geophysical Research Letters*, 29(14), 1693. <https://doi.org/10.1029/2002GL015311>.
- Grell, G.A. and Freitas, S.R. (2014) A scale and aerosol aware stochastic convective parameterization for weather and air quality modeling. *Atmospheric Chemistry and Physics*, 14(10), 5233–5250. <https://doi.org/10.5194/acp-14-5233-2014>.
- Gupta, S., Jain, I., Johari, P. and Lal, M. (2019) Impact of climate change on tropical cyclones frequency and intensity on Indian coasts. In: *Proceedings of International Conference on Remote Sensing for Disaster Management*. Cham: Springer. https://doi.org/10.1007/978-3-319-77276-9_32.
- Gutmann, E.D., Rasmussen, R.M., Liu, C., Ikeda, K., Bruyere, C.L., Done, J.M., Garré, L., Friis-Hansen, P. and Veldore, V. (2018) Changes in hurricanes from a 13-Yr convection-permitting pseudo-global warming simulation. *Journal of Climate*, 31(9), 3643–3657. <https://doi.org/10.1175/JCLI-D-17-0391.1>.
- Hemer, M.A. and Trenham, C.E. (2016) Evaluation of a CMIP5 derived dynamical global wind wave climate model ensemble. *Ocean Modelling*, 103, 190–203. <https://doi.org/10.1016/j.ocemod.2015.10.009>.
- Hersbach, H., Bell, B., Berrisford, P., Hirahara, S., Horányi, A., Muñoz-Sabater, J., Nicolas, J., Peubey, C., Radu, R., Schepers, D., Simmons, A., Soci, C., Abdalla, S., Abellán, X., Balsamo, G., Bechtold, P., Biavati, G., Bidlot, J., Bonavita, M., Chiara, G., Dahlgren, P., Dee, D., Diamantakis, M., Dragani, R., Flemming, J., Forbes, R., Fuentes, M., Geer, A., Haimberger, L., Healy, S., Hogan, R.J., Hölm, E., Janisková, M., Keeley, S., Laloyaux, P., Lopez, P., Lupu, C., Radnoti, G., Rosnay, P., Rozum, I., Vamborg, F., Villaume, S. and Thépaut, J. (2020) The ERA5 global reanalysis. *Quarterly Journal of the Royal Meteorological Society*, 146(730), 1999–2049. <https://doi.org/10.1002/qj.3803>.
- Hong, S.-Y., Dudhia, J. and Chen, S.-H. (2004) A revised approach to ice microphysical processes for the bulk parameterization of clouds and precipitation. *Monthly Weather Review*, 132(1), 103–120. [https://doi.org/10.1175/1520-0493\(2004\)132<0103: ARATIM>2.0.CO;2](https://doi.org/10.1175/1520-0493(2004)132<0103: ARATIM>2.0.CO;2).
- Hong, S.Y. and Lim, J.-O.J. (2006) The WRF single-moment 6-class microphysics scheme (WSM6). *Journal of Korean Meteorology Society*, 42, 129–151.
- Hong, S.-Y., Noh, Y. and Dudhia, J. (2006) A new vertical diffusion package with an explicit treatment of entrainment processes. *Monthly Weather Review*, 134(9), 2318–2341. <https://doi.org/10.1175/MWR3199.1>.
- Iacono, M.J., Delamere, J.S., Mlawer, E.J., Shephard, M.W., Clough, S.A. and Collins, W.D. (2008) Radiative forcing by long-lived greenhouse gases: calculations with the AER radiative transfer models. *Journal of Geophysical Research*, 113(D13), D13103. <https://doi.org/10.1029/2008JD009944>.
- IMD. (2019) *Cyclone eAtlas*. Chennai, India: Indian Meteorological Deptment. <http://14.139.191.203/Login.aspx>
- IMO. (2020) *Specialized products and services weather, Iran*. Tehran, Iran: IMO.
- IOWA State University. (2020) *ASOS-AWOS-METAR data download*. Ames, IA: IOWA State University. Available at: <https://mesonet.agron.iastate.edu/request/download.phtml>.
- Jiang, Z., Li, W., Xu, J. and Li, L. (2015) Extreme precipitation indices over China in CMIP5 models. Part I: model evaluation. *Journal of Climate*, 28(21), 8603–8619. <https://doi.org/10.1175/JCLI-D-15-0099.1>.
- Jiménez, P.A., Dudhia, J., González-Rouco, J.F., Navarro, J., Montávez, J.P. and García-Bustamante, E. (2012) A revised scheme for the WRF surface layer formulation. *Monthly Weather Review*, 140(3), 898–918. <https://doi.org/10.1175/MWR-D-11-00056.1>.
- Jisan, M.A., Bao, S., Pietrafesa, L.J., Shen, D., Gayes, P.T. and Hallstrom, J. (2018) Hurricane Matthew (2016) and its impact under global warming scenarios. *Modeling Earth Systems and Environment*, 4(1), 97–109. <https://doi.org/10.1007/s40808-018-0420-6>.
- Jones, J.J., Stephenson, T.S., Taylor, M.A. and Campbell, J.D. (2016) Statistical downscaling of North Atlantic tropical cyclone frequency and the amplified role of the Caribbean low-level jet in a warmer climate. *Journal of Geophysical Research: Atmospheres*, 121(8), 3741–3758. <https://doi.org/10.1002/2015JD024342>.
- Kain, J.S. (2004) The Kain-Fritsch convective parameterization: an update. *Journal of Applied Meteorology*, 43(1), 170–181. [https://doi.org/10.1175/1520-0450\(2004\)043<0170:TKCPAU>2.0.CO;2](https://doi.org/10.1175/1520-0450(2004)043<0170:TKCPAU>2.0.CO;2).
- Kalnay, E., Kanamitsu, M., Kistler, R., Collins, W., Deaven, D., Gandin, L., Iredell, M., Saha, S., White, G., Woollen, J., Zhu, Y., Leetmaa, A., Reynolds, R., Chelliah, M., Ebisuzaki, W.,

- Higgins, W., Janowiak, J., Mo, K.C., Ropelewski, C., Wang, J., Jenne, R. and Joseph, D. (1996) The NCEP/NCAR 40-year reanalysis project. *Bulletin of the American Meteorological Society*, 77(3), 437–471. [https://doi.org/10.1175/1520-0477\(1996\)077<0437:TNYRP>2.0.CO;2](https://doi.org/10.1175/1520-0477(1996)077<0437:TNYRP>2.0.CO;2).
- Katsube, K. and Inatsu, M. (2016) Response of tropical cyclone tracks to sea surface temperature in the western North Pacific. *Journal of Climate*, 29(5), 1955–1975. <https://doi.org/10.1175/JCLI-D-15-0198.1>.
- Knutson, T.R., McBride, J.L., Chan, J., Emanuel, K., Holland, G., Landsea, C., Held, I., Kossin, J.P., Srivastava, A.K. and Sugi, M. (2010) Tropical cyclones and climate change. *Nature Geoscience*, 3, 157–163.
- Knutson, T.R., Sirutis, J.J., Zhao, M., Tuleya, R.E., Bender, M., Vecchi, G.A., Villarini, G. and Chavas, D. (2015) Global projections of intense tropical cyclone activity for the late twenty-first century from dynamical downscaling of CMIP5/RCP4.5 scenarios. *Journal of Climate*, 28(18), 7203–7224. <https://doi.org/10.1175/JCLI-D-15-0129.1>.
- Lemos, G., Menendez, M., Semedo, A., Camus, P., Hemer, M., Dobrynin, M. and Miranda, P.M.A. (2020) On the need of bias correction methods for wave climate projections. *Global and Planetary Change*, 186, 103109. <https://doi.org/10.1016/j.gloplacha.2019.103109>.
- Lin, N., Emanuel, K., Oppenheimer, M. and Vanmarcke, E. (2012) Physically based assessment of hurricane surge threat under climate change. *Nature Climate Change*, 2(6), 462–467. <https://doi.org/10.1038/nclimate1389>.
- Mäll, M., Nakamura, R., Suursaar, Ü. and Shibayama, T. (2020) Pseudo-climate modelling study on projected changes in extreme extratropical cyclones, storm waves and surges under CMIP5 multi-model ensemble: Baltic Sea perspective. *Natural Hazards*, 102(1), 67–99. <https://doi.org/10.1007/s11069-020-03911-2>.
- Michaelis, A.C., Willison, J., Lackmann, G.M. and Robinson, W.A. (2017) Changes in winter North Atlantic extratropical cyclones in high-resolution regional pseudo-global warming simulations. *Journal of Climate*, 30(17), 6905–6925. <https://doi.org/10.1175/JCLI-D-16-0697.1>.
- Mittal, R., Tewari, M., Radhakrishnan, C., Ray, P., Singh, T. and Nickerson, A.K. (2019) Response of tropical cyclone Phailin (2013) in the Bay of Bengal to climate perturbations. *Climate Dynamics*, 53(3–4), 2013–2030. <https://doi.org/10.1007/s00382-019-04761-w>.
- Mlawer, E.J., Taubman, S.J., Brown, P.D., Iacono, M.J. and Clough, S.A. (1997) Radiative transfer for inhomogeneous atmospheres: RRTM, a validated correlated-k model for the longwave. *Journal of Geophysical Research: Atmospheres*, 102(D14), 16663–16682. <https://doi.org/10.1029/97JD00237>.
- Mori, N. and Takemi, T. (2016) Impact assessment of coastal hazards due to future changes of tropical cyclones in the North Pacific Ocean. *Weather and Climate Extremes*, 11, 53–69. <https://doi.org/10.1016/j.wace.2015.09.002>.
- Morim, J., Hemer, M., Andutta, F., Shimura, T. and Cartwright, N. (2020) Skill and uncertainty in surface wind fields from general circulation models: Intercomparison of bias between AGCM, AOGCM and ESM global simulations. *International Journal of Climatology*, 40(5), 2659–2673. <https://doi.org/10.1002/joc.6357>.
- Morim, J., Hemer, M., Cartwright, N., Strauss, D. and Andutta, F. (2018) On the concordance of 21st century wind-wave climate projections. *Global and Planetary Change*, 167(2017), 160–171. <https://doi.org/10.1016/j.gloplacha.2018.05.005>.
- Murakami, H., Sugi, M. and Kitoh, A. (2013) Future changes in tropical cyclone activity in the north Indian Ocean projected by high-resolution MRI-AGCMs. *Climate Dynamics*, 40(7–8), 1949–1968. <https://doi.org/10.1007/s00382-012-1407-z>.
- Murakami, H., Vecchi, G.A. and Underwood, S. (2017) Increasing frequency of extremely severe cyclonic storms over the Arabian Sea. *Nature Climate Change*, 7(12), 885–889. <https://doi.org/10.1038/s41558-017-0008-6>.
- Nakamura, R., Shibayama, T., Esteban, M. and Iwamoto, T. (2016) Future typhoon and storm surges under different global warming scenarios: case study of typhoon Haiyan (2013). *Natural Hazards*, 82(3), 1645–1681. <https://doi.org/10.1007/s11069-016-2259-3>.
- Nayak, S. and Takemi, T. (2019) Dynamical downscaling of typhoon lionrock (2016) for assessing the resulting hazards under global warming. *Journal of the Meteorological Society of Japan*, 97(1), 69–88. <https://doi.org/10.2151/jmsj.2019-003>.
- NCEI GIS Agile Team. (2020) *Hourly/sub hourly observational data map*. Asheville, NC: NCEI GIS Agile Team. Available at: <https://www.ncei.noaa.gov/maps/hourly/>.
- Ninomiya, J., Mori, N., Takemi, T. and Arakawa, O. (2017) SST ensemble experiment-based impact assessment of climate change on storm surge caused by pseudo-global warming: case study of typhoon Vera in 1959. *Coastal Engineering Journal*, 59(2), 1–20. <https://doi.org/10.1142/S0578563417400022>.
- Parvathi, V., Suresh, I., Lengaigne, M., Izumo, T. and Vialard, J. (2017) Robust projected weakening of winter monsoon winds over the Arabian Sea under climate change. *Geophysical Research Letters*, 44(19), 9833–9843. <https://doi.org/10.1002/2017GL075098>.
- Rajeevan, M., Srinivasan, J., Niranjan Kumar, K., Gnanaseelan, C. and Ali, M.M. (2013) On the epochal variation of intensity of tropical cyclones in the Arabian Sea. *Atmospheric Science Letters*, 14(4), 249–255. <https://doi.org/10.1002/asl2.447>.
- Saha, S., Moorthi, S., Pan, H.-L., Wu, X., Wang, J., Nadiga, S., Tripp, P., Kistler, R., Woollen, J., Behringer, D., Liu, H., Stokes, D., Grumbine, R., Gayno, G., Wang, J., Hou, Y.-T., Chuang, H., Juang, H.-M.H., Sela, J., Iredell, M., Treadon, R., Kleist, D., Van Delst, P., Keyser, D., Derber, J., Ek, M., Meng, J., Wei, H., Yang, R., Lord, S., van den Dool, H., Kumar, A., Wang, W., Long, C., Chelliah, M., Xue, Y., Huang, B., Schemm, J.-K., Ebisuzaki, W., Lin, R., Xie, P., Chen, M., Zhou, S., Higgins, W., Zou, C.-Z., Liu, Q., Chen, Y., Han, Y., Cucurull, L., Reynolds, R.W., Rutledge, G. and Goldberg, M. (2010) The NCEP climate forecast system reanalysis. *Bulletin of the American Meteorological Society*, 91(8), 1015–1058. <https://doi.org/10.1175/2010BAMS3001.1>.
- Sajjad, M., Lin, N. and Chan, J.C.L. (2020) Spatial heterogeneities of current and future hurricane flood risk along the U.S. Atlantic and Gulf coasts. *Science of the Total Environment*, 713, 136704. <https://doi.org/10.1016/j.scitotenv.2020.136704>.
- Sattar, A.M. and Cheung, K.K.W. (2019) Comparison between the active tropical cyclone seasons over the Arabian Sea and Bay of Bengal. *International Journal of Climatology*, 39(14), 5486–5502. <https://doi.org/10.1002/joc.6167>.
- Schulzweida, U. (2019) *CDO User Guide (Version 1.9.8)*. Hamburg, Germany: Max-Planck Institute for Meteorology.
- Soltanpour, M., Ranji, Z., Shibayama, T. and Ghader, S. (2021) Tropical cyclones in the Arabian Sea: overview and simulation

- of winds and storm-induced waves. *Natural Hazards*, 108, 711–732. <https://doi.org/10.1007/s11069-021-04702-z>.
- Strachan, J., Vidale, P.L., Hodges, K., Roberts, M. and Demory, M. E. (2013) Investigating global tropical cyclone activity with a hierarchy of AGCMs: the role of model resolution. *Journal of Climate*, 26(1), 133–152. <https://doi.org/10.1175/JCLI-D-12-00012.1>.
- Taylor, K.E. (2001) Summarizing multiple aspects of model performance in a single diagram. *Journal of Geophysical Research: Atmospheres*, 106(D7), 7183–7192. <https://doi.org/10.1029/2000JD900719>.
- Tewari, M., Chen, F., Wang, W., Dudhia, J., LeMone, M.A., Mitchell, K., Ek, M., Gayno, G., Wegiel, J. and Cuenca, R.H. (2004) Implementation and verification of the unified NOAH land surface model in the WRF model. In: *20th Conference on Weather Analysis and Forecasting/16th Conference on Numerical Weather Prediction*. Seattle, WA: American Meteorological Society.
- Thompson, C., Barthe, C., Bielli, S., Tulet, P. and Pianezze, J. (2021) Projected characteristic changes of a typical tropical cyclone under climate change in the Southwest Indian Ocean. *Atmosphere*, 12(2), 1–19. <https://doi.org/10.3390/atmos12020232>.
- Thompson, G., Field, P.R., Rasmussen, R.M. and Hall, W.D. (2008) Explicit forecasts of winter precipitation using an improved bulk microphysics scheme. Part II: implementation of a new snow parameterization. *Monthly Weather Review*, 136(12), 5095–5115. <https://doi.org/10.1175/2008MWR2387.1>.
- Walsh, K.J.E., Camargo, S.J., Knutson, T.R., Kossin, J., Lee, T.C., Murakami, H. and Patricola, C. (2018) Tropical cyclones and climate change. *Tropical Cyclone Research and Review*, 8(4), 240–250. <https://doi.org/10.1016/j.tcrr.2020.01.004>.
- Wang, B., Xu, S. and Wu, L. (2012) Intensified Arabian Sea tropical storms. *Nature*, 489, E1–E2. <https://doi.org/10.1038/nature11470>.
- Zarifsanayei, A.R., Antolínez, J.A.A., Etemad-Shahidi, A., Cartwright, N. and Strauss, D. (2022) *Coastal Engineering*, 104080. <https://doi.org/10.1016/j.coastaleng.2022.104080>
- Zha, J., Wu, J., Zhao, D. and Fan, W. (2020) Future projections of the near-surface wind speed over eastern China based on CMIP5 datasets. *Climate Dynamics*, 54(3–4), 2361–2385. <https://doi.org/10.1007/s00382-020-05118-4>.
- Zhang, Y., Wang, Y., Chen, Y., Liang, F. and Liu, H. (2019) Assessment of future flash flood inundations in coastal regions under climate change scenarios—a case study of Hadahe River basin in northeastern China. *Science of the Total Environment*, 693, 133550. <https://doi.org/10.1016/j.scitotenv.2019.07.356>.

SUPPORTING INFORMATION

Additional supporting information may be found in the online version of the article at the publisher's website.

How to cite this article: Ranji, Z., Zarifsanayei, A. R., Cartwright, N., & Soltanpour, M. (2022). Climate change impacts on tropical cyclones of the Arabian Sea: Projections and uncertainty investigations. *International Journal of Climatology*, 42(10), 5121–5141. <https://doi.org/10.1002/joc.7523>